

A 2 mm spectral line survey of the starburst galaxy NGC 253

S. Martín

*Instituto de Radioastronomía Milimétrica (IRAM), Avda. Divina Pastora 7, Local 20,
E-18012 Granada, Spain*

`martin@iram.es`

R. Mauersberger

*Instituto de Radioastronomía Milimétrica (IRAM), Avda. Divina Pastora 7, Local 20,
E-18012 Granada, Spain*

J. Martín-Pintado

*Departamento de Astrofísica Molecular e Infrarroja, Instituto de Estructura de la Materia,
CSIC, Serrano 121, E-28006 Madrid, Spain*

C. Henkel

Max-Planck-Institut für Radioastronomie, Auf dem Hügel 69, D-53121 Bonn, Germany

and

S. García-Burillo

Observatorio de Madrid, Alfonso XII, 3, 28014 Madrid, Spain

ABSTRACT

We present the first unbiased molecular line survey towards an extragalactic source, namely the nuclear region of the starburst galaxy NGC 253. The scan covers the frequency band from 129.1 to 175.2 GHz, i.e. most of the 2 mm atmospheric window. We identify 111 spectral features as transitions from 25 different molecular species. Eight of which (three tentatively) are detected for the first time in the extragalactic interstellar medium. Among these newly detected species, we detected the rare isotopomers ^{34}SO and HC^{18}O^+ . Tentative detections of two deuterated species, DNC and N_2D^+ , are reported for the first time from a target beyond the Magellanic Clouds. Additionally, three hydrogen recombination lines are identified, while no organic molecules larger than methanol are detected. Column densities and rotation temperatures are calculated for all

the species, including an upper limit to the ethanol abundance. A comparison of the chemical composition of the nuclear environment of NGC 253 with those of selected nearby galaxies demonstrates the chemical resemblance of IC 342 and NGC 4945 to that of NGC 253. On the other hand, the chemistries characterizing NGC 253 and M 82 are clearly different. We also present a comparison of the chemical composition of NGC 253 with those observed in Galactic prototypical sources. The chemistry of NGC 253 shows a striking similarity with the chemistry observed toward the Galactic center molecular clouds, which are thought to be dominated by low-velocity shocks. This resemblance strongly suggests that the heating in the nuclear environment of NGC 253 is dominated by the same mechanism as that in the central region of the Milky Way.

Subject headings: surveys — galaxies: abundances — galaxies: individual (NGC 253) — galaxies: ISM — galaxies: nuclei — galaxies: starburst — radio lines: galaxies

1. Introduction

Our knowledge of the chemical composition of the interstellar medium (ISM) in the nuclei of external galaxies has so far been restricted to only ~ 30 molecular species (see Sect. 4.1), which is still far from the 129 molecules detected in the interstellar and circumstellar medium within our Galaxy (Lovas 2004). The initial detection of most of these 129 molecules has been the result of unbiased frequency scans towards specific Galactic sources, such as massive star-forming regions (e.g. Sgr B2(M), Cummins et al. 1986; OriMC-1, Lee et al. 2001), cold molecular clouds (e.g. TMC-1, Kaifu et al. 2004), and evolved stars (e.g. IRC+10216, Cernicharo et al. 2000). Spectral line scans towards Galactic sources focused mainly on the hot cores associated with massive star-forming regions such as Sgr B2 and Orion-KL due to their complex chemistry as well as the brightness of their lines. Extragalactic molecular spectroscopy has been so far limited to selecting the strongest features seen in the Galactic center and disk sources and observing them towards well selected extragalactic targets. The most ambitious census of the molecular content of an external galaxy is the compilation of data toward the starburst galaxy NGC 4945 by Wang et al. (2004). Their multi-line study combines observations of 19 molecular species previously known in other extragalactic sources.

Up to now unbiased molecular line surveys of extragalactic sources do not exist in spite of providing a powerful tool for determining the physical parameters of the molecular ISM. Observations of a large number of molecular lines with similar angular resolution allow us

to describe the chemical complexity of the source which provides fundamental information on the physical processes heating the medium in heavily obscured regions. Additionally, frequency scans lead to serendipitous detections of new species.

The nuclear starburst of the galaxy NGC 253, the target of this survey, is one of the brightest and most prolific (in terms of molecular line detections) extragalactic molecular line sources. The Sculptor galaxy NGC 253 is an almost edge-on barred spiral ($i = 72^\circ - 78^\circ$, Puche et al. 1991; Pence 1981) classified as type SAB(s)c (de Vaucouleurs et al. 1991) or Sc(s) (Sandage & Tammann 1987). At a distance of ~ 3 Mpc (e.g. Mouhcine et al. 2005), NGC 253 is one of the nearest archetypes of nuclear starburst galaxies (Rieke et al. 1980). Its nuclear region contains one of the brightest extragalactic IRAS sources with a $100\mu\text{m}$ flux of 1860 Jy (Soifer et al. 1989). In fact, most of the overall IR luminosity of this galaxy ($L_{\text{IR}} = 2.1 \cdot 10^{10} L_\odot$, $SFR_{\text{IR}} = 3.6 M_\odot \text{yr}^{-1}$, Strickland et al. 2004) stems from the regions of intense massive star formation within its central few hundred parsecs. Violent massive star formation is also revealed by the high supernova rate of $0.05 - 0.3 \text{yr}^{-1}$ in the nuclear region of this galaxy (Mattila & Meikle 2001; Ulvestad & Antonucci 1997).

The high nuclear star formation activity is driven by huge amounts of molecular gas in the central few hundred parsecs of NGC 253 ($1.3 - 2.6 \cdot 10^9 M_\odot$, Canzian et al. 1988; Mauersberger et al. 1996), likely powered by the bar structure first detected at near-infrared wavelengths (Scoville et al. 1985; Forbes & DePoy 1992). Position-velocity diagrams from high-resolution observations of the nuclear region of NGC 253 show that the molecular material seems to follow orbital motions around the dynamical center which are interpreted as x_1 and x_2 orbits within the context of a bar-like potential (OH, Turner 1985; CO, Canzian et al. 1988; Das et al. 2001; Paglione et al. 2004; HCN, Paglione et al. 1995; CS, Peng et al. 1996; SiO, H^{13}CO^+ , García-Burillo et al. 2000).

Here we present the first unbiased molecular line survey carried out towards a source outside the Milky Way. Technically, this survey was driven by the availability of two new wideband (1 GHz) receivers at 2 mm and new 1 GHz wide filter bank spectrometers, together with the large collecting area of the IRAM 30 m telescope. Species such as NO, NS, SO_2 , H_2S and H_2CS , detected for the first time towards a starburst environment, were previously reported by Martín et al. (2003, 2005). Additional new molecules together with a full analysis of the data are presented.

2. Observations and results

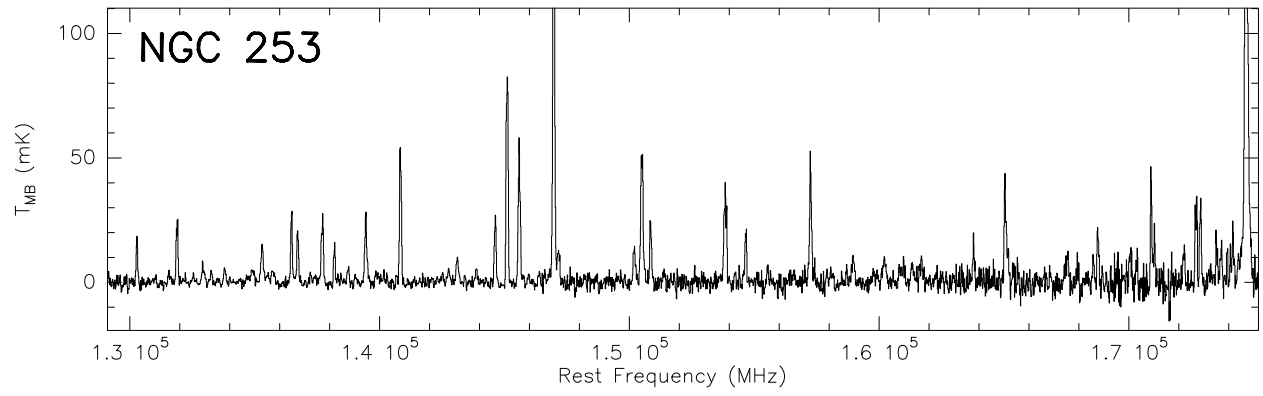


Fig. 1.— Complete 2 mm spectral frequency scan toward the nuclear region of NGC 253.

The first molecular frequency scan of an external galaxy was carried out at 2 mm with the 30 m IRAM telescope at Pico Veleta, Spain, between 2001 and 2004. It covers $\sim 86\%$ of the observable 2 mm atmospheric window, from 129.1 to 175.2 GHz (Fig. 1). At these frequencies, the telescope beamwidth ranges from $19''$ to $14''$. Fig. 2 shows the size of the 30 m beam on top of an interferometric map of SiO emission (García-Burillo et al. 2000). A *K*-band image of NGC 253 (Engelbracht et al. 1998) is displayed in grey-scale to illustrate the size of the observed region relative to the galaxy.

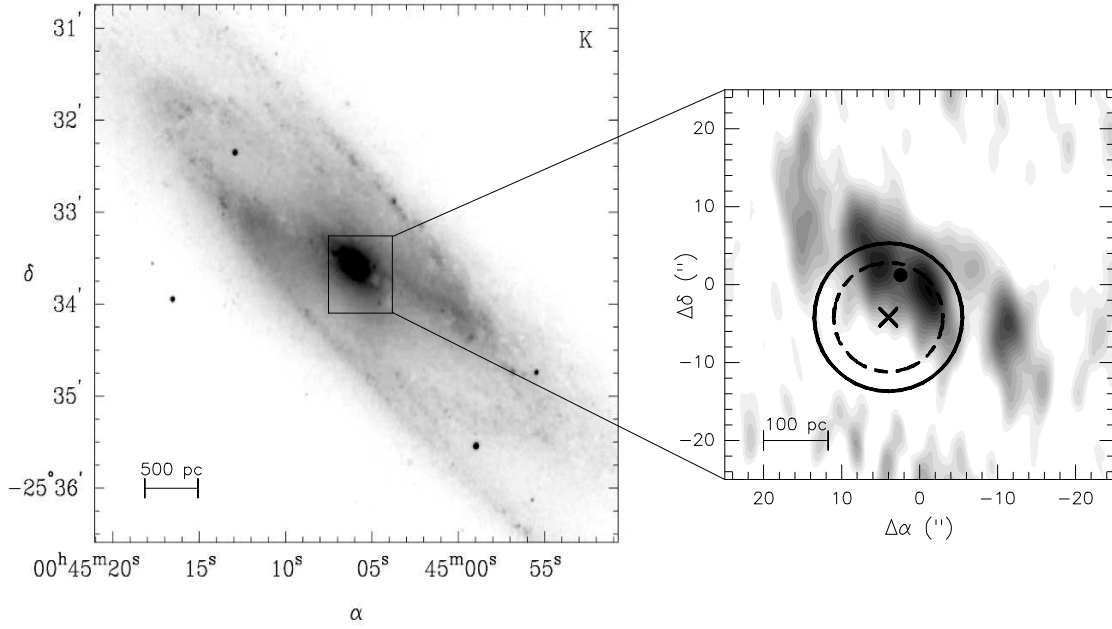


Fig. 2.— Grey-scale, K -band image of NGC 253 (left panel, Engelbracht et al. 1998) and high-resolution SiO emission (right panel, García-Burillo et al. 2000). Beam sizes of the IRAM 30 m telescope for the extreme frequencies observed in the survey are shown as circles on top of the SiO map. The continuous line shows the $19''$ beam at 129 GHz and the dashed line the $14''$ beam at 175 GHz. A cross indicates the nominal position of the 2 mm scan in this work and a dot the dynamical center as derived by García-Burillo et al. (2000).

The observations were pointed at the position $\alpha_{\text{J2000}} = 00^{\text{h}}47^{\text{m}}33^{\text{s}}.3$, $\delta_{\text{J2000}} = -25^{\circ}17'23''$. This position is $\sim 6''$ south-east of the dynamical center of NGC 253. A pointing accuracy of $\sim 3''$ was achieved by measuring cross-scans on nearby continuum sources every ~ 2 hours. The observations were carried out in a wobbler-switching mode with a symmetrical beam throw of $4'$ in azimuth and a switching frequency of 0.5 Hz.

Each of the two available SIS receivers working at 2 mm with orthogonal polarizations provides a 1 GHz bandwidth. The receivers were tuned to adjacent frequencies, with an overlap of 100 MHz, to cover an instantaneous bandwidth of 1.9 GHz for each frequency setup. As spectrometers we used two 256×4 MHz filterbanks, providing a velocity resolution between 7 and 9 km s^{-1} at the observed frequencies.

The rejection of the image band (the upper side band) was typically ~ 10 dB so that only the very few strongest lines were also detected from the image band. The image sideband rejection was calculated for each frequency setup (lower panel in Fig. 3) by measuring the difference in power between a hot and a cold load, first with full rejection of the upper side band and then with full rejection of the lower side band by using a Martin-Puplett interferometer. The image gain is then computed as the ratio between these two measurements. We assume this gain ratio to be constant throughout the whole 1 GHz frequency band covered by each backend.

The spectra were calibrated with a standard dual load system. The temperature scale of the spectra is in T_{MB} obtained as

$$T_{\text{MB}} = (F_{\text{eff}}/B_{\text{eff}})T_{\text{A}}^*, \quad (1)$$

where the forward efficiency (F_{eff}) is 0.93 at 2 mm. The beam efficiency was calculated for each frequency with the Ruze function,

$$B_{\text{eff}} = 1.2\epsilon \exp[-(4\pi R\sigma/\lambda)^2], \quad (2)$$

using $\epsilon = 0.69$, $R\sigma = 0.07$ and λ in mm.

At the latitude of Pico Veleta Observatory, NGC 253 is at elevations $> 20^\circ$ only for about four hours. A complete observing session with about 120 minutes effective observing time was spent on each frequency setup, out of which half the time was spent on source. The integration time for each frequency setup is shown in the central panel of Fig. 3.

The observing mode combined with the stability of the system provided high quality baselines. Only linear baselines were subtracted from the spectra. The rms of the residuals after subtracting the fitted line profiles on each frequency setup is shown in the upper panel of Fig. 3. The values are mostly of order of 2–4 mK in $\sim 8 \text{ km s}^{-1}$ wide channels, increasing up to ~ 6 –10 mK at the highest measured frequencies.

In the scanned 46 GHz wide band we have detected a total of 111 lines, the weakest of which have an intensity of ~ 3 mK. The spectral density of detected lines is 2.4 features/GHz. Since the Doppler linewidth in NGC 253 is about 200 km s^{-1} , or 100 MHz, we are not limited by line blending, but by a lack of sensitivity. For targeted searches with longer integration time it may still be possible to detect and identify lines at levels of ≤ 1 mK.

Fig. 4 shows the full 2 mm spectral line scan of NGC 253 with the line identifications superposed on the spectra. In Table 1 we are listing the parameters derived from Gaussian fits to the detected lines. We identify 25 molecular species and 3 hydrogen recombination lines.

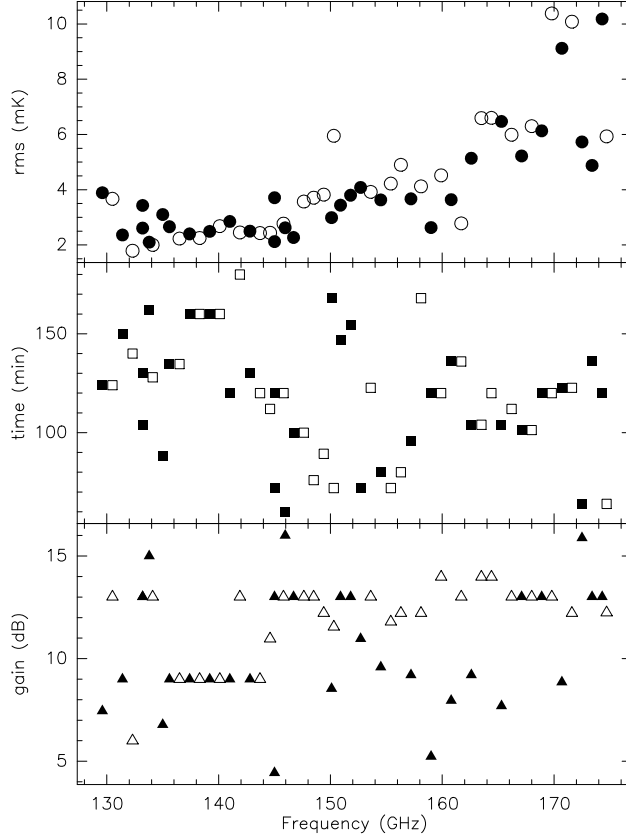


Fig. 3.— Summary of the observational parameters of individual frequency setups. Open and filled symbols refer to each of the 2 mm SIS receivers. *Upper panel:* rms of the spectrum in $7\text{--}9\text{ km s}^{-1}$ wide channels in T_{mb} after subtracting a linear baseline; *Central panel:* Total integration time which includes the time spent on the reference position; *Lower panel:* Measured rejection of the image (upper) sideband.

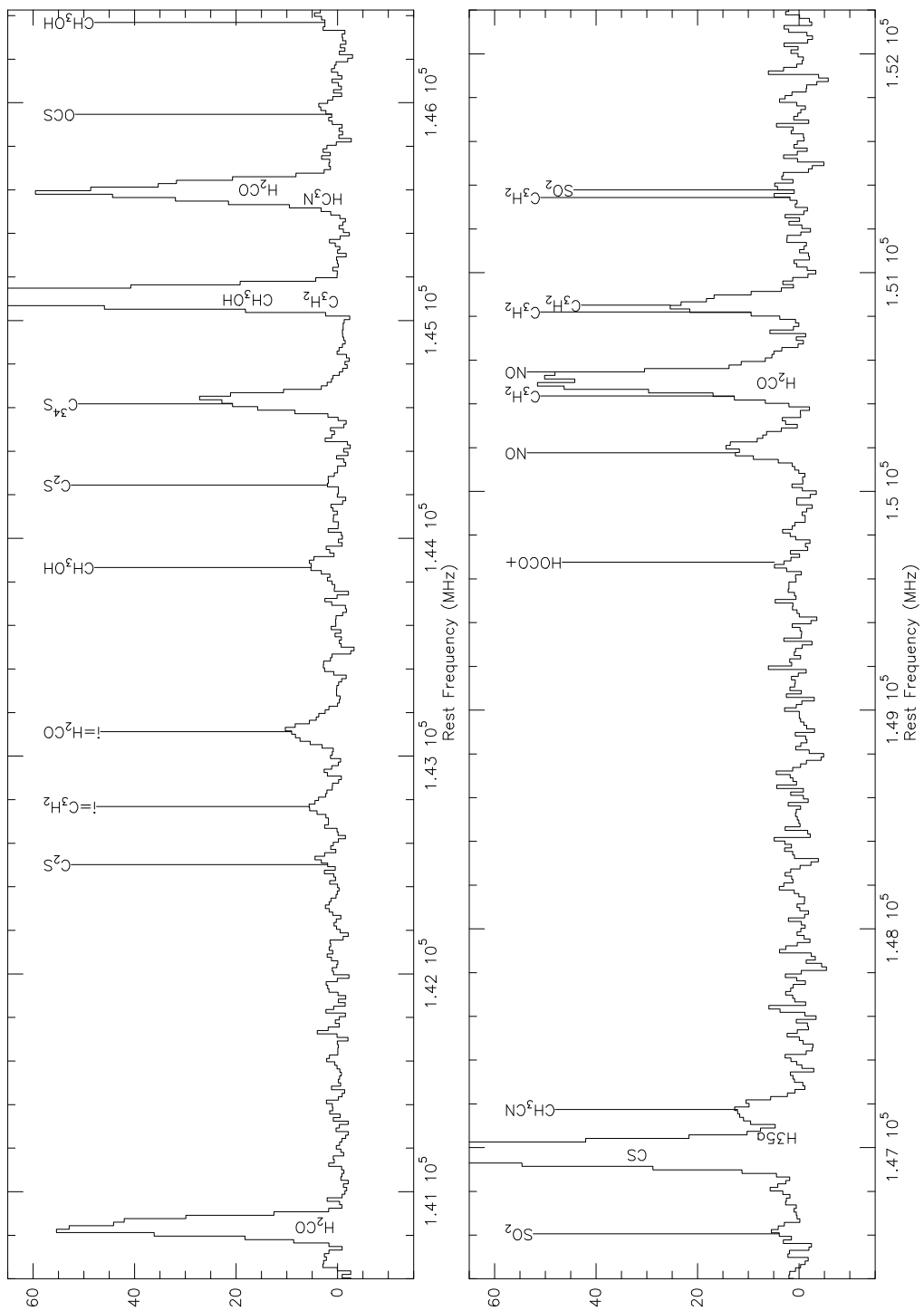


Fig. 4. — (Cont.)

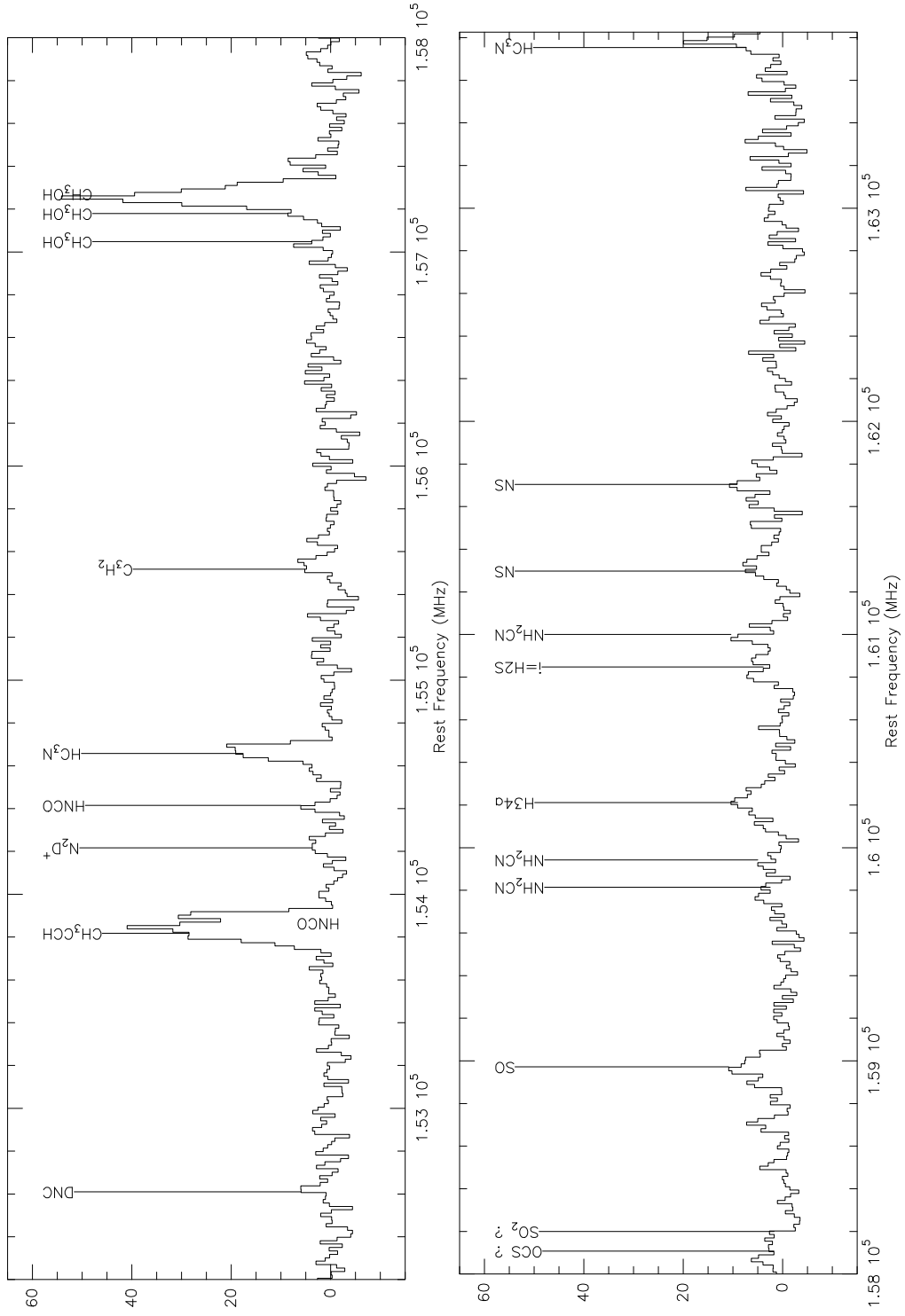


Fig. 4. — (Cont.)

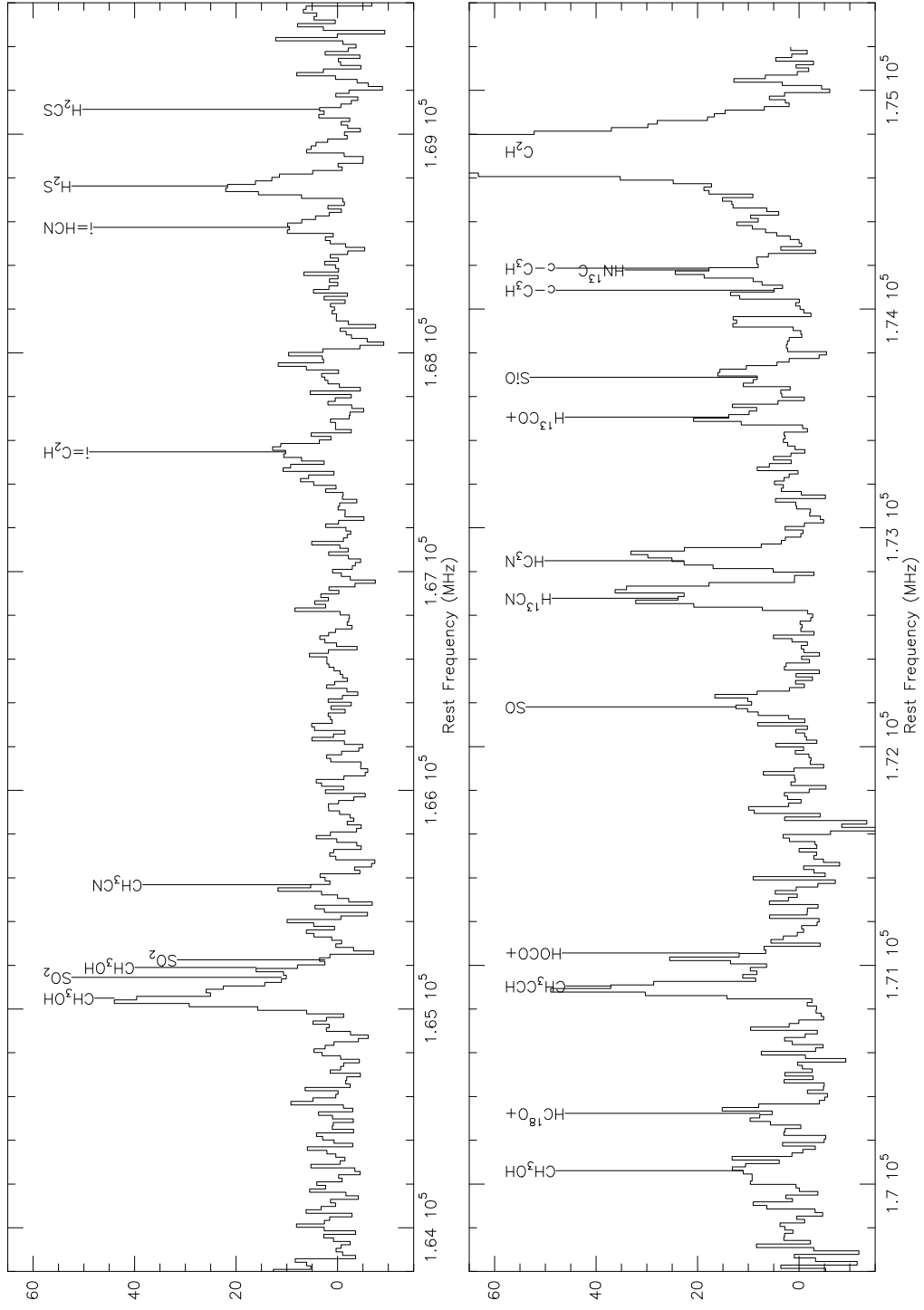


Fig. 4. — (Cont.)

Table 1: Results from Gaussian fits to the observed lines

Molecule Transition	ν (MHz)	note	$\int T_{\text{MB}} dv$ mK km s ⁻¹	V_{LSR} km s ⁻¹	$\Delta v_{1/2}$ km s ⁻¹	T_{MB} mK
SiO 3 – 2 $v=0$	130268.6		1580 (50)	183	76	18
			1170 (50)	260	91	12
C₂S 11 ₁₀ – 10 ₉	131551.9		640 (90)	230	151	4.0
HNCO 60,6 – 50,5	131885.7		2400 (150)	182	72	32
			2000 (180)	284	80	24
CH₂NH 2 _{1,1} – 1 _{1,0}	133272.1	hf	420 (40)	187	83 ^b	4.8
			450 (40)	283	83 ^b	5.1
OCS 11 – 10	133785.9		1220 (130)	212	200	5.8
SO₂ 8 _{2,6} – 8 _{1,7}	134004.8		300 (70)	242	91	3.1
H36α	135286.0	b s	2800 (...)	250 ^a	282 ^a	9.3
H₂CS 4 _{1,4} – 3 _{1,3}	135297.8	b	1040 (90)	221	158	6.2
SO₂ 5 _{1,5} – 4 _{0,4}	135696.0		740 (160)	245 ^a	140 ^a	4.2
³⁴SO 4 ₃ – 3 ₂	135775.3	b	300 (60)	180 ^a	73 ^a	3.8
		b	200 (70)	274 ^a	88 ^a	2.1
HC₃N 15-14	136464.4		2410 (130)	183	77	29
			2000 (300)	271	85	22
CH₃CCH 8 _k – 7 _k	136728.0		3410 (110)	255	158	20
SO 4 ₃ – 3 ₂	138178.5		1400 (200)	180	73	18
			1100 (200)	274	88	12
¹³CS 3 – 2	138739.3		550 (70)	188	70 ^b	7.4
			390 (50)	274	70 ^b	5.2
NH₂CN 7 _{1,7} – 6 _{1,6}	139032.0		580 (110)	280 ^a	155 ^a	3.5
H₂CS 4 _{1,3} – 3 _{1,2}	139483.4	b	1340 (150)	221	176	7.2
NH₂CN 7 _{0,7} – 6 _{0,6}	139842.1		490 (160)	280 ^a	155 ^a	3.0
NH₂CN 7 _{0,7} – 6 _{0,6}	139954.4	m	520 (160)	279	140	3.5
C₂S 10 ₁₁ – 9 ₁₀	140180.7		470 (130)	250	85	5.2
SO₂ 6 _{2,4} – 6 _{1,5}	140306.1		510 (60)	248	115	4.1
H₂CO 2 _{1,2} – 1 _{1,1}	140839.5		4250 (140)	186	104 ^b	38
			6050 (150)	288	104 ^b	55
C₂S 11 ₁₁ – 10 ₁₀	142501.7		430 (70)	192	85 ^a	4.7
CH₃OH 3 _{1,3} – 2 _{1,2} A+	143865.7		1000 (130)	225	168	5.6
C₂S 12 ₁₁ – 11 ₁₀	144244.8		290 (120)	210	112	2.4
C³⁴S 3 – 2	144617.1		3000 (300)	188	105	27
			1500 (300)	284	86	16
c-C₃H₂ 3 _{1,2} – 2 _{2,1}	145089.5	b s	1750 (...)	234 ^a	156 ^a	11
CH₃OH 3-2	145103.2	b m	9400 (200)	185	115	77
			5760 (190)	294	96	57
HC₃N 16-15	145560.9	b s	2100 (...)	183 ^a	77 ^a	26
		b s	1700 (...)	271 ^a	85 ^a	19
H₂CO 2 _{0,2} – 1 _{0,1}	145602.9	b	3400 (100)	177	90 ^b	35
		b	3300 (100)	283	90 ^b	34

Table 1: (Cont.)

Molecule Transition	ν (MHz)	note	$\int T_{\text{MB}} dv$ mK km s ⁻¹	V_{LSR} km s ⁻¹	$\Delta v_{1/2}$ km s ⁻¹	T_{MB} mK
OCS 12 – 11	145946.8		580 (170)	212 ^a	210 ^a	2.6
CH₃OH 3 _{1,2} – 2 _{1,2} A – –	146368.3		1020 (150)	196	139	6.9
SO₂ 4 _{2,2} – 4 _{1,3}	146605.5		800 (170)	241	148	5.1
CS 3 – 2	146969.0	b	11900 (200)	185	100	111
		b	13700 (200)	288	117	110
H35α	147046.8	b s	2800 (...)	250 ^a	282 ^a	9.3
CH₃CN 8 _k – 7 _k	147174.5	b m	2040 (180)	258	165	12
HOCO⁺ 7 _{0,7} – 6 _{0,6}	149675.8		410 (110)	281	68	5.6
NO $\frac{3}{2} - \frac{1}{2} \Pi^+$	150176.5	hf	3400 (500)	244	158	10
c-C₃H₂ 2 _{2,0} – 1 _{1,1}	150436.5	b s	600 (...)	234 ^a	156 ^a	3.6
H₂CO 2 _{1,1} – 1 _{1,0}	150498.3	b	5300 (100)	180	99 ^b	50
		b	5100 (100)	286	99 ^b	48
NO $\frac{3}{2} - \frac{1}{2} \Pi^-$	150546.5	hf b s	3400 (...)	244 ^a	158 ^a	10
c-C₃H₂ 4 _{0,4} – 3 _{1,3}	150820.6	b	1150 (...)	234 ^b	156 ^b	7.0
c-C₃H₂ 4 _{1,4} – 3 _{0,3}	150851.9	b	3380 (110)	234 ^b	156 ^b	20
c-C₃H₂ 5 _{1,4} – 5 _{0,5}	151343.8	b s	165 (...)	234 ^a	156 ^a	1.0
SO₂ 2 _{2,0} – 2 _{1,1}	151378.6	b	590 (170)	225	158	3.5
DNC 2 – 1	152609.7		490 (160)	225	61	7.5
CH₃CCH 9 _k – 8 _k	153817.2	b	4300 (200)	271	157	26
HNCO 7 _{0,7} – 6 _{0,6}	153865.0		2660 (150)	183	72	34
		b s	2240 (...)	284 ^a	80 ^a	26
N₂D⁺ 2 – 1	154217.0		570 (170)	219	120	4.5
HNCO 7 _{1,6} – 6 _{1,5}	154414.7		540 (110)	283 ^a	80 ^a	6.4
HC₃N 17-16	154657.3		1640 (120)	191	72 ^b	21
			1400 (110)	272	72 ^b	18
c-C₃H₂ 3 _{2,2} – 2 _{1,1}	155518.2		820 (180)	205	118	6.6
CH₃OH 6 _{0,6} – 6 _{-1,6} E	157048.6		540 (120)	275	103 ^b	5.0
CH₃OH 5 _{0,5} – 5 _{-1,5} E	157178.9	b	960 (150)	242	103 ^b	8.8
CH₃OH $J_{0,k} - J_{-1,k}$ E	157270.7	b m	2110 (160)	183	103 ^b	19
$J = 1..4; k = J$			5700 (200)	290	103 ^b	52
SO 3 ₄ – 2 ₃	158971.7		700 (200)	180 ^a	92	7.2
		b	1000 (200)	274 ^a	84	11
NH₂CN 8 _{0,8} – 7 _{0,7}	159814.6		750 (180)	283 ^b	155 ^b	4.5
NH₂CN 8 _{0,8} – 7 _{0,7}	159942.7	m	700 (200)	283 ^b	158 ^b	4.1
H34α	160211.5		2800 (200)	250	282	9.3
NH₂CN 8 _{1,7} – 7 _{1,6}	161000.3	b	1430 (170)	280	155 ^a	8.6
NS $\frac{7}{2} - \frac{5}{2} e$	161297.2	hf	1800 (500)	199	224	3.1
NS $\frac{7}{2} - \frac{5}{2} f$	161697.2	hf	2400 (400)	249	278	3.4
HC₃N 18-17	163753.4		1500 (400)	185 ^a	73	20
			700 (300)	272 ^a	98	6.6

Table 1: (Cont.)

Molecule Transition	ν (MHz)	note	$\int T_{\text{MB}} dv$ mK km s ⁻¹	V_{LSR} km s ⁻¹	$\Delta v_{1/2}$ km s ⁻¹	T_{MB} mK
CH₃OH $J_{1,k-1} - J_{0,k}$ E	165050.1	b m	1700 (400)	169	72	22
$J = 1..3; k = J$			4700 (400)	273	100	45
SO₂ $5_{2,4} - 5_{1,5}$	165144.6	b s	640 (...)	248 ^a	115 ^a	5.2
CH₃OH $4_{1,3} - 4_{0,4}$ E	165190.5	b	900 (200)	291	90 ^a	9.1
SO₂ $7_{1,7} - 6_{0,6}$	165225.4	b s	900 (...)	248 ^a	115 ^a	7.4
CH₃CN $9_k - 8_k$	165568.9	b m	1200 (300)	258 ^a	166 ^a	7.0
H₂S $1_{1,0} - 1_{0,1}$	168762.7		1520 (180)	180	100	14
			2250 (80)	275	88	24
H₂CS $5_{1,5} - 4_{1,4}$	169113.5		970 (200)	270	165 ^a	5.5
CH₃OH $3_{2,3} - 2_{1,3}$	170060.6		2400 (400)	248	178	12
HC¹⁸O⁺ $2 - 1$	170322.7		500 (300)	206	46	11
			500 (200)	285	49	10
CH₃CCH $10_k - 9_k$	170905.6		5100 (500)	275	102	47
HOCO⁺ $8_{0,8} - 7_{0,7}$	171055.9	b	1700 (300)	295	66	25
SO $4_4 - 3_3$	172181.4		1300 (300)	180 ^a	87	14
			900 (300)	274 ^a	74	11
H¹³CN $2_k - 1_k$	172677.9	hf	3200 (200)	181	74	40
			2400 (200)	279	66	34
HC₃N 19-18	172849.3		2800 (400)	184	74	35
			1800 (400)	269	75	22
H¹³CO⁺ $2 - 1$	173506.7		860 (90)	170	60 ^b	14
			1450 (100)	269	60 ^b	23
SiO $4 - 3$ v=0	173688.3		1070 (110)	184 ^a	76 ^a	13
			1000 (120)	270 ^a	91 ^a	10
c-C₃H $3_{1,2} - 2_{1,1}$	174086.1	hf	900 (200)	180 ^a	41 ^b	6.5
			1600 (500)	280 ^a	40	12
HN¹³C $2 - 1$	174179.4		1050 (170)	271	60	16
C₂H $2 - 1$	174663.2	hf	30000 (6000)	162	108	82
			27000 (6000)	282	104	88

Note. — (see Appendix A for details):

b - Blended line.

s - Synthetic Gaussian to isolate a given feature. See text for details on the parameters used for deriving these profiles for each species.

hf - Hyperfine structure. Frequency and intensity refers to the main component of the group.

m - Multi-transition line. Frequency refers to the main component of the group.

^aParameter fixed in the Gaussian fit

^bParameters forced to have the same value in the Gaussian fit

Table 2: Physical parameters derived for all detected species. Source averaged column densities, rotation temperature and abundances relative to H₂.

Molecule		N^a (cm ⁻²)	T_{rot} (K)	$[X]/[H_2]^b$ ($\times 10^{-9}$)
SiO	180 km s ⁻¹	5.0(1.0) 10 ¹²	7.4(0.7)	0.07
	270 km s ⁻¹	3.6(0.9) 10 ¹²	8.7(1.2)	0.05
C ₂ S		1.4(1.2) 10 ¹³	24(9)	0.2
NH ₂ CN		1.2(0.5) 10 ¹³	67(13)	0.2
CH ₃ CN		2.0(0.6) 10 ¹³	9.6(0.7)	0.3
c-C ₃ H	130 km s ⁻¹	8.1(1.6) 10 ¹²	12	0.1
	280 km s ⁻¹	1.5(0.3) 10 ¹³	12	0.2
c-C ₃ H ₂		3.0(6.0) 10 ¹³	9(8)	0.4
NS ^c		4.3(0.6) 10 ¹³	7.2(1.0)	0.6
HC ₃ N	180 km s ⁻¹	1.8(0.5) 10 ¹³	33(4)	0.3
	270 km s ⁻¹	1.9(0.6) 10 ¹³	24(3)	0.3
HOCO ⁺		2.6(1.8) 10 ¹³	12	0.4
H ₂ CS		4.4(4.5) 10 ¹³	11(4)	0.6
SO ₂		5.0(2.0) 10 ¹³	15(2)	0.7
H ₂ S	180 km s ⁻¹	2.3(1.1) 10 ¹³	12	0.3
	275 km s ⁻¹	3.5(1.4) 10 ¹³	12	0.5
CH ₂ NH	190 km s ⁻¹	2.5(1.1) 10 ¹³	12	0.4
	300 km s ⁻¹	2.8(0.9) 10 ¹³	12	0.4
HNC ^c	270 km s ⁻¹	7.2(1.2) 10 ¹³	12	1
SO	180 km s ⁻¹	4.5(3.3) 10 ¹³	40(24)	0.7
	270 km s ⁻¹	3.1(2.8) 10 ¹³	34(24)	0.5
HNCO	180 km s ⁻¹	5.7(2.7) 10 ¹³	23(6)	0.8
	280 km s ⁻¹	4.8(2.5) 10 ¹³	23	0.7
HCO ⁺ ^c	170 km s ⁻¹	3.9(0.8) 10 ¹³	12	0.6
	270 km s ⁻¹	6.4(1.2) 10 ¹³	12	1
H ₂ CO	180 km s ⁻¹	6.9(0.9) 10 ¹³	27(2)	1
	285 km s ⁻¹	9.0(1.7) 10 ¹³	34(4)	1
OCS ^d		2.5(0.3) 10 ¹⁴	17(2)	4
HCN ^c	180 km s ⁻¹	1.8(0.3) 10 ¹⁴	12	2
	280 km s ⁻¹	1.4(0.2) 10 ¹⁴	12	2
CS ^{c,d}	180 km s ⁻¹	2.0(0.2) 10 ¹⁴	9.7(0.4)	3
	280 km s ⁻¹	1.4(0.2) 10 ¹⁴	10.0(0.2)	2
CH ₃ CCH		4.3(0.2) 10 ¹⁴	63(20)	6
CH ₃ OH		8.3(0.3) 10 ¹⁴	11.6(0.2)	12
C ₂ H	160 km s ⁻¹	6.8(1.1) 10 ¹⁴	12	10
	280 km s ⁻¹	5.6(0.9) 10 ¹⁴	12	8
NO ^d		4.0(0.4) 10 ¹⁵	6(2)	60

^aErrors derived from the rotation diagrams without beam filling factor considerations (see Sect. 3.3).

^bAssumed $N(H_2) = 6.7 \times 10^{22} \text{ cm}^{-2}$. See Table 6.

^cCalculated from the observed ¹³C isotope transition with ¹²C/¹³C ~ 40 from Henkel et al. (1993).

^dUsing additional transitions measured by Martín et al. (2003, 2005).

3. Data analysis

3.1. Line identification and fitting

In order to identify and fit the observed features we have used the rest frequencies from the molecular line catalogs of Lovas (1992, 2004) and Pickett et al. (1998). The existing molecular line surveys towards the Galactic center sources Sgr B2(OH) (Cummins et al. 1986; Turner 1989, 1991) and Sgr B2(N, M and NW) (Nummelin et al. 1998, 2000) were also used as additional information to estimate the expected intensity of the fainter identified lines not included in the Lovas (2004) catalog.

One of the main difficulties in identifying lines from single dish observations of extragalactic sources stems from their large width, typically $\geq 100 \text{ km s}^{-1}$. In addition, the emission lines from the nuclear region of NGC 253 show two velocity components, roughly at 180 and 280 km s^{-1} , with linewidths of ~ 100 and 110 km s^{-1} respectively (from CS, Martín et al. 2005). These components arise from the two main molecular lobes separated by $10''$ and located on both sides of the nucleus. As a consequence, some of the observed transitions will appear partially or totally blended. Table 1 shows the results of the Gaussian fits to all the molecular transitions identified towards the NGC 253 nuclear region. In the third column of Table 1 we have included a note to indicate whether the transition is affected by blending. Appendix A describes the fitting procedures used for the different types of blending found in our spectral line survey.

3.2. Column density determination

From the observed main beam brightness temperature of the measured molecular lines one can estimate column densities and rotation temperatures (T_{rot}) for each species (see Appendix B.1 for a detailed discussion). All the necessary spectroscopic information required to derive these parameters (i.e. A_{ul} , ν , g_u , E_u and Z in Eq. B6) were extracted or derived from the JPL catalog (Pickett et al. 1998).

In order to derive T_{rot} and to extrapolate the column densities in the observed states to a total column density for a given molecule, more than one transition has to be measured. In the case that only one transition was detected in the 2 mm scan, an educated guess of the rotation temperature was made (see Appendix C).

Table 2 shows the derived total column densities and rotation temperatures for the detected species in NGC 253. Source averaged abundances are also given, where a source averaged molecular hydrogen column density $N(\text{H}_2) = 6.7 \cdot 10^{22} \text{ cm}^{-2}$ has been assumed (see

Sect. 4.4.1).

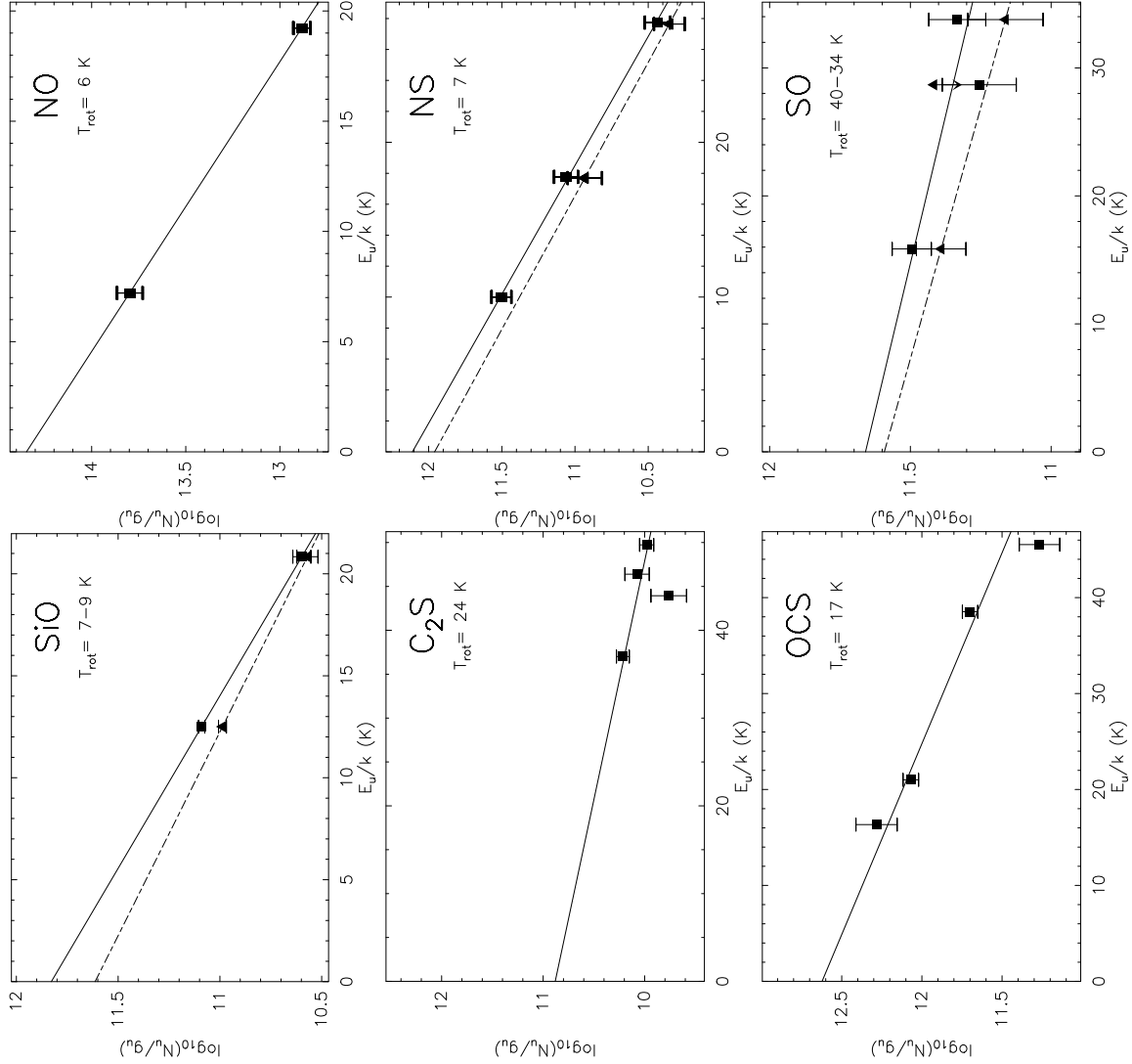


Fig. 5.— Rotation diagrams of detected species. When differentiated, velocity components are represented as filled squares and solid lines (180 km s^{-1}) and filled triangles and dashed lines (270 km s^{-1}). Unfilled markers represent blended observed transitions whose intensities have been estimated by inter- or extrapolation from the diagrams (see Appendix A for details). The NS, NO and OCS diagrams include additional transitions observed by Martín et al. (2003, 2005).

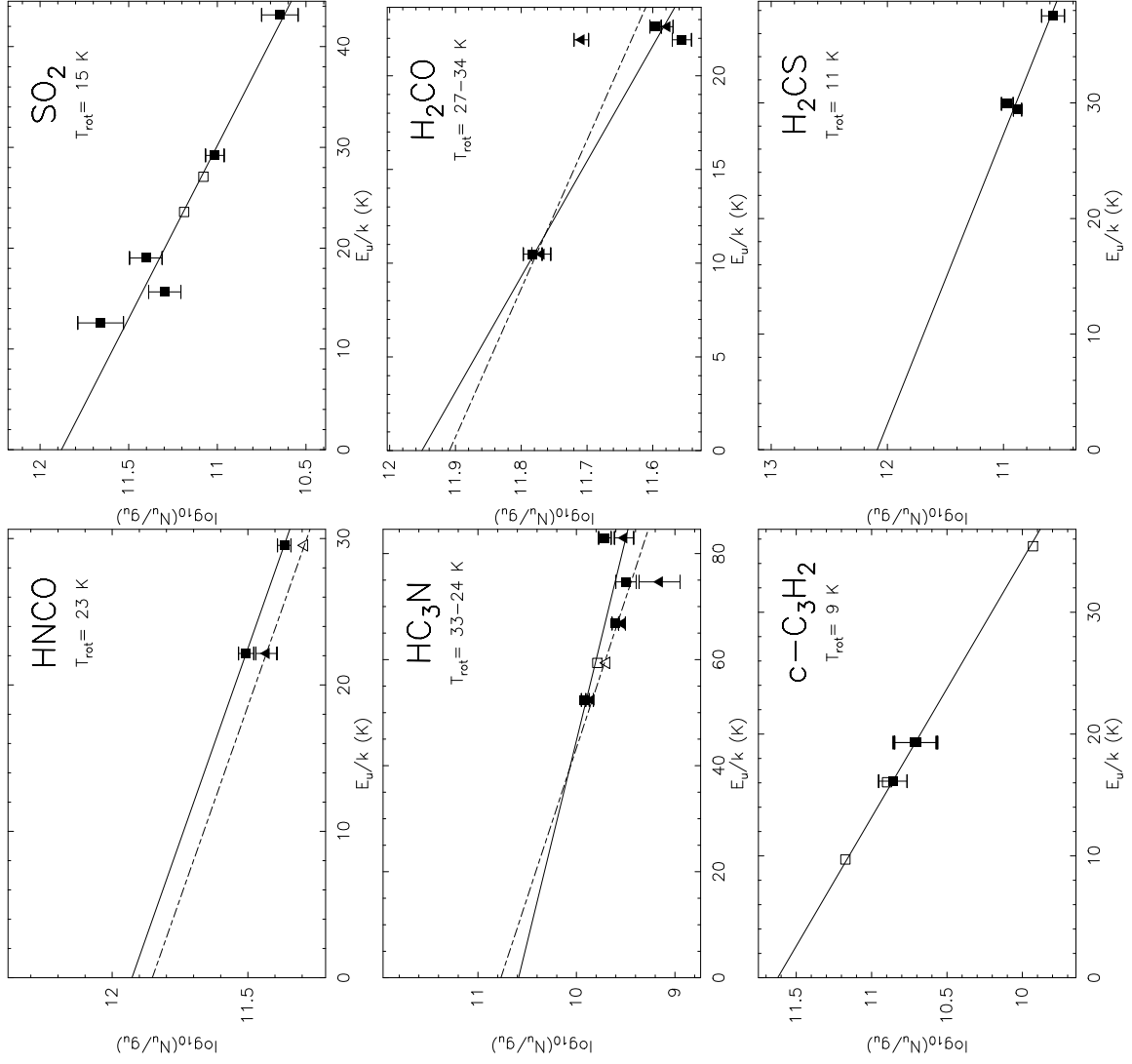


Fig. 5. — (Cont.)

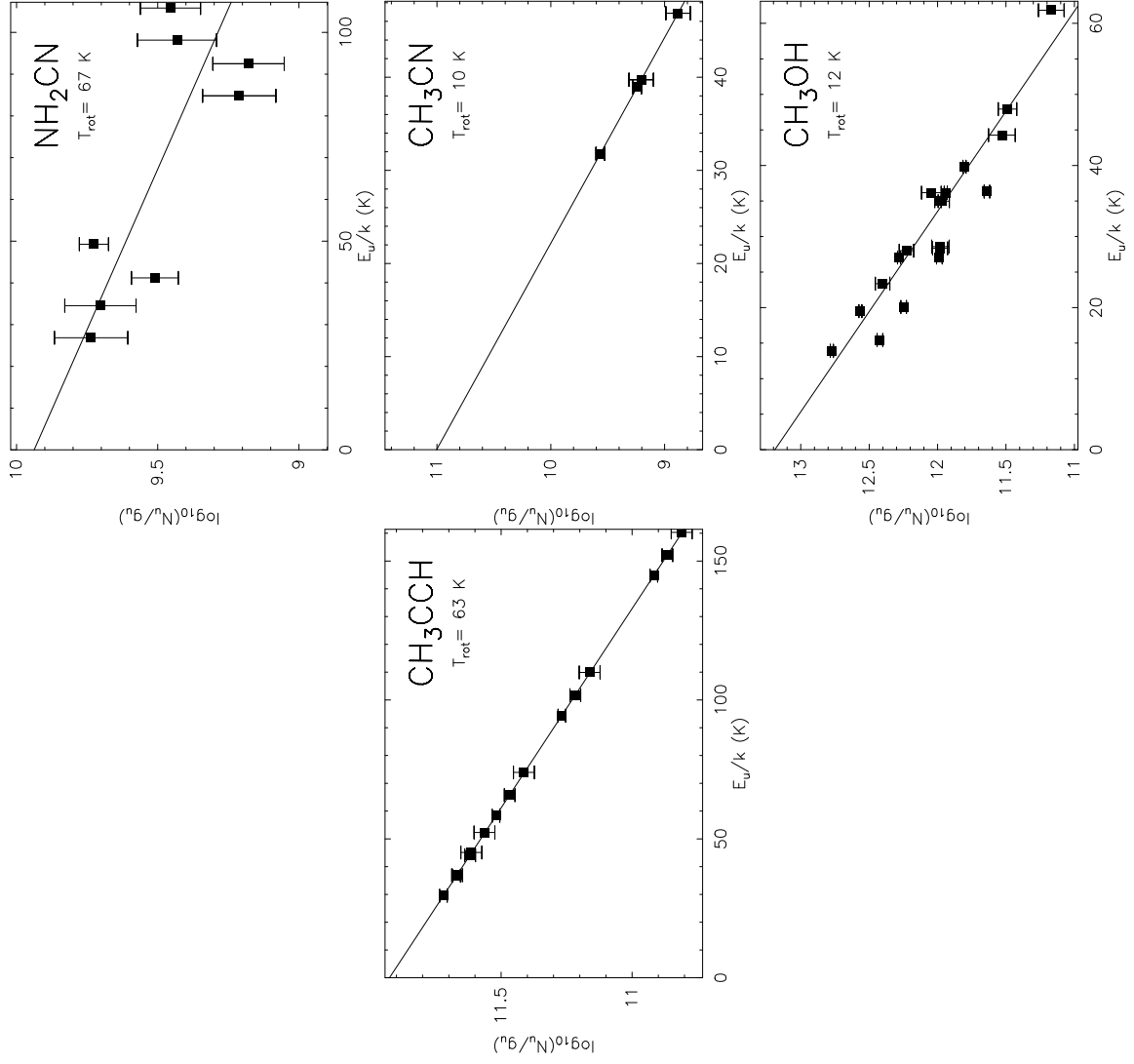


Fig. 5. — (Cont.)

3.3. Uncertainty in column densities and rotation temperatures

The main source of uncertainty, when deriving the column densities and rotation temperatures, arises from the uncertainty of the extent of the emitting regions.

The source averaged brightness temperature (T_B) can be estimated from the measured main beam brightness temperature as

$$T_B = \eta_{bf}^{-1} T_{MB} \quad (3)$$

where, in the approximation of a Gaussian source distribution of size θ_s observed with a Gaussian beam of size θ_b , the beam filling factor $\eta_{bf} = \theta_s^2 / (\theta_s^2 + \theta_b^2)$ accounts for the dilution effect due to the coupling between the source and the telescope beam.

In order to correct for beam dilution in the nuclear region of NGC 253, Mauersberger et al. (2003) smoothed the high resolution interferometric CS map from Peng et al. (1996) to convert the three observed transitions of CS by Mauersberger & Henkel (1989) to a common angular resolution of $32''$. Since we know the intensities of the CS lines with the original resolution (T_{MB}) and those corrected to a $32''$ beam ($T_{MB}^{32''}$) we can derive the beam filling factor. From the expression $\eta_{bf}^{32''} T_{MB} = \eta_{bf} T_{MB}^{32''}$ we estimate the extent of the emitting region to be $\theta_s = 23''$, $21''$ and $19''$ for the CS $J = 2 - 1$, $J = 3 - 2$ and $J = 5 - 4$ transitions respectively. In our analysis we will then consider an equivalent source size of $20''$ to convert our main beam brightness temperature to source averaged brightness temperature.

The other main source of uncertainty stems from the assumption that all the observed species arise from the same volume. The only way to confirm this would be high-resolution observations of different transitions of several species. The interferometric map of the $J = 2 - 1$ line of CS by Peng et al. (1996) shows that most of the emission of this molecule is concentrated within a radius of $\sim 20''$. The CS emission is seen to be clumped into four large main molecular cloud complexes symmetrically distributed with respect to the dynamical center and roughly aligned with the molecular bar. A recent high-resolution multiline study carried out towards IC 342 (Meier & Turner 2005) shows clear differences in the distribution of several important molecular tracers. Towards NGC 253, however, high-resolution maps of molecular transitions requiring different excitation conditions such as HCN, CO, SiO, $H^{13}CO^+$ and NH_3 (Paglione et al. 1995, 2004; García-Burillo et al. 2000; Ott et al. 2005) show very similar distributions, in good agreement with that of CS. Therefore it is plausible that for NGC 253, as long as the bulk of the emission arises from the area confined by the starburst, the extent of the emission of different molecules is similar.

We now address the question of how an error in the assumed source size will affect our determination of physical parameters. As derived from Eq. B1 (see Appendix B.1), the

calculated total column density is affected by the filling factor through T_B . The upper panel in Fig 6 shows the variation of the inverse of the filling factor (i.e. the conversion factor from T_{MB} to T_B from Eq. 3) as a function of source size, normalized to the value for a source of $20''$. This value represents, in a first approximation, the factor by which we should multiply our derived column densities if the source extent would be different from that assumed. We have considered the extreme cases of the beam sizes at 129 and 175 GHz. The grey shaded area corresponds to source sizes between $10''$ and $30''$ where we expect the source size to be confined. In case of a source size larger than $20''$ column densities would be overestimated by only $\sim 20\%$, while for sizes down to $10''$, the column density would be underestimated by less than a factor of 2. Only in case of an extremely clumped and compact emission where source sizes were well below $10''$, column densities would be dramatically affected. We have also considered the effect of source size on the derived rotation temperature from rotation diagrams. We will assume a case in which we derive $T_{rot} = 15$ K (for a $20''$ source) by observing two transitions of a given species at 129 and 175 GHz respectively. In the lower panel in Fig. 6 we have plotted the relative change in the derived T_{rot} for those cases where the transitions would have upper levels with an energy difference of 60, 30 and 15 K. It is obvious that the more affected T_{rot} is that derived from the data with the smaller dynamical range in energies. From Fig. 6 we see that the largest expected uncertainty in the determination of T_{rot} is smaller than 20%.

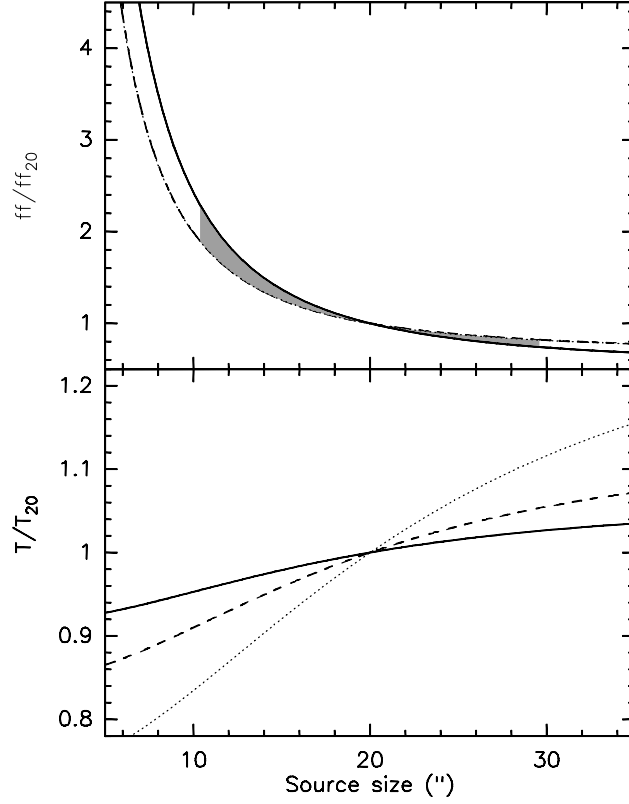


Fig. 6.— *Upper panel:* Variation of the filling factor normalized to that corresponding to a source extent of $20''$ as a function of source size. The continuous line corresponds to the beam at 129 GHz and the dashed line to the beam at 175 GHz. The shaded area highlights values with source sizes between 10 and $30''$. *Lower panel:* Effect of the assumed source size on the rotation temperature determined from rotation diagrams relative to the assumed $T_{\text{rot}} = 15\text{K}$ for $\theta_s = 20''$ with two transitions measured at 129 and 175 GHz where the involved levels are separated by 60 (continuous line), 30 (dashed line) and 15 K (dotted line).

4. Discussion

4.1. Extragalactic molecular census

Table 3 lists the detection of all the species known to date in the extragalactic ISM in chronological order. During the last three decades, 29 molecules and 11 rare isotopic substitutions have been detected outside the Galaxy. As a result of the frequency scan presented in this paper (see also Martín et al. 2003, 2005), 8 new molecules and 2 isotope (shown in boldface in Table 3) have been added to the census of known extragalactic species, which represents a $\sim 30\%$ increase in the total number of identified molecules. While H_2S and H_2CS were detected towards the nearby Large Magellanic Cloud (Heikkilä et al. 1999), their identification in our survey (see Martín et al. 2005) represents the first detections towards a starburst galaxy. Note that CH_2NH , HOCO^+ and C_3H (Table 3) are tentatively detected and need confirmation by observations of additional transitions. In Table 3 the known extragalactic species not detected in the 2 mm band are shown in italics.

Table 3: Known extragalactic molecules (see Sect. 4.1)

Molecule	Publication Year	Telescope	Ref.
<i>OH</i>	1971	OVRO	1
H ₂ CO	1974	64 m	2
<i>CO</i>	1975	11 m	3
¹³ <i>CO</i>	1975	11 m	4
<i>H₂O</i>	1977	100 m	5
<i>HCN</i>	1977	11 m	6
<i>H₂</i>	1978	2.3 m	7
<i>NH₃</i>	1979	100 m	8
<i>HCO</i> ⁺	1979	7 m	9
<i>CH</i>	1980	64 m	10
CS	1985	7 m	11
C ₃ H ₂	1986	43 m	12
<i>CH</i> ⁺	1987	1.4 m	13
CH ₃ OH	1987	30 m	14
<i>CN</i>	1988	30 m	15
C ₂ H	1988	30 m	15
<i>HNC</i>	1988	30 m	15
HC ₃ N	1988	30 m	15,16
HNCO	1989	30 m	17,18
C ³⁴ S	1989	30 m	19
<i>C</i> ¹⁸ <i>O</i>	1991	11 m/30 m	20
<i>C</i> ¹⁷ <i>O</i>	1991	11 m/30 m	20
SO	1991	15 m	21
<i>N₂H</i> ⁺	1991	30 m	22
SiO	1991	30 m	22
H ¹³ CO ⁺	1991	30 m	22
HN ¹³ C	1991	30 m	22
<i>H</i> ¹³ <i>CN</i>	1991	30 m	22
CH ₃ CCH	1991	30 m	23
CH ₃ CN	1991	30 m	23
¹³ CS	1993	30 m	24
OCS	1995	30 m	25
<i>HCO</i>	1995	12 m	26
DCO ⁺	1996	15 m	27
DCN	1996	15 m	27
<i>HC</i> ¹⁵ <i>N</i>	1999	15 m	28
H ₂ S	1999	15 m	29
H ₂ CS	1999	15 m/30 m	29,30
<i>CO</i> ⁺	2000	30 m	31

Table 3: (Cont.)

Molecule	Publication Year	Telescope	Ref.
SO₂	2003	30 m	32
NO	2003	30 m	32
NS	2003	30 m	32
³⁴SO	2003	30 m	32
<i>HOC⁺</i>	2004	30 m	33
C₂S	2006	30 m	34
CH₂NH	2006	30 m	34
NH₂CN	2006	30 m	34
HOCO⁺	2006	30 m	34
C₃H	2006	30 m	34
HC¹⁸O⁺	2006	30 m	34

Note. — Table adapted and updated from Mauersberger & Henkel (1993)
In roman: molecules observed in this survey; In **boldface**: molecular species not previously identified outside the Milky Way; In *italics*: species not measured in this survey.
Telescopes.- (OVRO) Owens Valley interferometer; (64 m) Parkes 64 m; (11 m) NRAO Kitt Peak 11 m; (100 m) Effelsberg 100 m; (2.3 m) Steward observatory 2.3 m; (7 m) AT&T Bell Labs 7 m; (43 m) NRAO Green Bank 43 m; (1.4 m) ESO 1.4 m Coudé; (30 m) IRAM Pico Veleta 30 m; (15 m) ESO SEST 15 m;

References. — (1) Weliachew (1971); (2) Gardner & Whiteoak (1974); (3) Rickard et al. (1975); (4) Solomon & de Zafra (1975); (5) Churchwell et al. (1977); (6) Rickard et al. (1977); (7) Thompson et al. (1978); (8) Martin & Ho (1979); (9) Stark & Wolff (1979); (10) Whiteoak et al. (1980); (11) Henkel & Bally (1985); (12) Seaquist & Bell (1986); (13) Magain & Gillet (1987); (14) Henkel et al. (1987); (15) Henkel et al. (1988); (16) Mauersberger et al. (1990); (17) Nguyen-Q-Rieu et al. (1989); (18) Nguyen-Q-Rieu et al. (1991); (19) Mauersberger & Henkel (1989); (20) Sage et al. (1991); (21) Johansson (1991); (22) Mauersberger & Henkel (1991); (23) Mauersberger et al. (1991); (24) Henkel et al. (1993); (25) Mauersberger et al. (1995); (26) Sage & Ziurys (1995); (27) Chin et al. (1996); (28) Chin et al. (1999); (29) Heikkilä et al. (1999); (30) Martín et al. (2005); (31) Fuente et al. (2000); (32) Martín et al. (2003); (33) Usero et al. (2004); (34) This work.

4.2. Deuterated molecules in NGC 253

The observation of deuterated molecules in external galaxies is interesting for several reasons. The interstellar D/H ratio depends on the degree of processing of the gas, since D was mainly produced soon after the big bang while nuclear processes during stellar evolution rather destroy than form deuterium. A low D/H ratio may therefore indicate that the observed gas component has been recycled in stars, and a higher ratio could be a hint for recent infall of poorly processed material. It has been observed that D is strongly enriched (by a factor of $> 10^4$ compared to the cosmic D/H ratio) in several molecules observable at cm- and mm-wavelengths. From model calculations, such a high degree of fractionation is expected if the molecules are being formed in a relatively cool ($T_{\text{kin}} < 30$ K) environment (e.g. Millar 2002, and references therein). The fact that a high enrichment of deuterated molecules is also observed in hot molecular cores can be explained by evaporation of molecules from grain mantles (e.g. Pineau des Forêts et al. 1989). While a value of $3(\pm 0.4) 10^{-5}$ has been estimated for the primordial D/H ratio (Burles 2002, and references therein), a lower ratio of $1.4(\pm 0.24) 10^{-5}$ is found in the Galactic neighborhood, and variations are shown on larger scales (Vidal-Madjar 2002). In molecular clouds close to the center of the Milky Way, Jacq et al (1999) find DCN and DCO⁺ enhancements which are compatible with a D/H an order of magnitude smaller than toward the local interstellar medium. This indicates that the gas in the Galactic center region is highly processed. The enhancement of deuterated molecules in the Large Magellanic Cloud, on the other hand, is compatible with the local value of the D/H ratio (Chin et al. 1996). No deuterated molecules have been detected so far toward the central regions of other galaxies. Mauersberger et al. (1995) give an upper limit for the DCN/HCN abundance ratio of $4 10^{-3}$ toward NGC 253.

Our survey includes the $J = 2-1$ lines of DCO⁺, DCN, DNC and N₂D⁺. All other 2 mm lines of deuterated molecules are expected to be much weaker. Table 4 shows the frequencies of these lines, the rms noise and limits or values of the integrated intensities. DCO⁺ and DCN are not detected. There is a tentative feature at the frequency of DNC and a more significant feature at the line frequency of N₂D⁺. At the frequencies of DNC $J = 2-1$ no line from another molecule is expected to be strong enough to explain the observed emission. Close to the frequencies of N₂D⁺ $J = 2-1$ is the transition frequency of OC³⁴S $J = 13-12$ (at 154.242 GHz). However, from our detections of OCS and our estimates of the ³²S/³⁴S ratio (Martín et al. 2005), this emission is expected to be an order of magnitude weaker than what is observed. Another potentially blending line is the $7_{1,6}-6_{1,5}, v_6 = 1$ transition of vibrationally excited HNCO (at 154.228 GHz). This line has been detected toward the Galactic hot core G10.47+0.03 with an intensity of about 1/5 that of the corresponding HNCO ground state transition, compatible with a kinetic temperature of about 380 K (Wyrowski et al. 1999). The feature we are observing here is about as strong as the HNCO $7_{1,6}-6_{1,5}$ ground vibrational

state transition (Table 1). If the feature at 154.228 GHz comes from vibrationally excited HNC O this would either indicate a higher kinetic temperature or maser emission. Both would be remarkable in view of the large volume observed in our beam toward NGC 253. While all this suggests that we have detected, for the first time, one or two deuterated molecules beyond the Magellanic Clouds, we will nevertheless regard the measured features as tentative.

Table 4: Parameters of selected deuterated species

Molecule	Transition $J - J'$	ν (MHz)	rms ^a (mK)	$\int T_{\text{MB}} dv$ ^b (K km s ⁻¹)	[DX]/[HX]
DCO ⁺	2 – 1	144077.3	1.9	<0.30	< 4 10 ⁻³ ^c
DCN	2 – 1	144827.9	1.1	<0.18	< 1 10 ⁻³ ^c
DNC	2 – 1	152609.7	3.1	0.49	≤ 1 10 ⁻² ^c
N ₂ D ⁺	2 – 1	154217.0	2.8	0.57	≤ 1.4 10 ⁻³ ^d

Note. — See Sect. 4.2 for details.

^arms computed for 20 km s⁻¹ wide channels.

^b3 σ limit to the integrated intensity assuming a linewidth of 150 km s⁻¹. DNC and N₂D⁺ detections are tentative.

^cUsing the ¹³C bearing species measured in this survey and assuming ¹²C/¹³C \sim 40 (Henkel et al. 1993).

^dUsing the $J = 1 - 0$ N₂H⁺ transition from Mauersberger & Henkel (1991).

Table 4 gives limits to the $[DX]/[HX]$ column density ratios for HCO^+ , HCN and HNC based on our limits for the $J = 2 - 1$ transitions of the deuterated isotopomers, the integrated intensities of the ^{13}C bearing isotopomers measured in this survey and the $^{12}\text{C}/^{13}\text{C}$ ratio of 40 obtained by Henkel et al. (1993). We have assumed that the excitation conditions of the deuterated and main species are similar. Intensities were corrected to account for beam dilution assuming a source size of $20''$ (see also Sect. 3.3). For N_2D^+ , we have only the N_2H^+ $J = 1 - 0$ line for a comparison (Mauersberger & Henkel 1991). The value for the $\text{N}_2\text{D}^+/\text{N}_2\text{H}^+$ column density ratio given in Table 4 assumes optically thin emission, making the same assumptions on the excitation as they have been made for DCN in the appendix of Mauersberger et al. (1995).

We obtain limits to the $[DX]/[HX]$ values of $4 \cdot 10^{-3}$ for HCO^+ , of $1 \cdot 10^{-3}$ for HCN and $11 \cdot 10^{-3}$ for HNC . These limits are two orders of magnitude above the local interstellar D/H ratio and an order of magnitude larger than the $[\text{DCN}]/[\text{HCN}]$ ratios estimated for Sgr B2 (Jacq et al 1999), but an order of magnitude lower than the values determined by Chin et al. (1996) in the Large Magellanic Cloud. The limits are consistent with the high kinetic temperatures determined toward the molecular interstellar medium of NGC 253. We can exclude the scenario found in many Galactic hot cores, where recent grain mantle evaporation leads to high D/H ratios that were preserved from a time when the temperature of the gas was much lower than now.

4.3. Alcohols in NGC 253

In the nuclear region of the Milky Way widespread large abundances of the methanol (CH_3OH) and ethanol ($\text{C}_2\text{H}_5\text{OH}$) alcohols have been reported (Requena-Torres et al. 2005; Martín-Pintado et al. 2001). This fact has motivated a careful search for the presence of $\text{C}_2\text{H}_5\text{OH}$ in the 2 mm scan. Table 5 shows the frequencies and energies of its 14 brightest 2 mm transitions assuming $T_{\text{rot}} = 12 \text{ K}$, as that derived for methanol (see Table 2). We have computed the rms of the noise for 20 km s^{-1} velocity resolution whenever the transition appeared not to be contaminated by other spectral features. From this rms, we estimate a 3σ detection limit to the integrated intensity of the transitions. With the limit to the detection of the 152 GHz transition we derive an upper limit to the ethanol column density of $N(\text{C}_2\text{H}_5\text{OH}) < 1.8 \cdot 10^{14} \text{ cm}^{-2}$. This limit to the column density can be improved if we add up all the transitions which appear not to be blended. We estimate a total column density limit of $N(\text{C}_2\text{H}_5\text{OH}) < 9.6 \cdot 10^{13} \text{ cm}^{-2}$.

The methanol to ethanol abundance ratio derived for NGC 253 is ≥ 10 . This lower limit is still a factor of 2 below the ratios derived for the GC clouds by Requena-Torres et al.

(2005). Thus, further high sensitivity observations are required to establish if the methanol to ethanol abundance ratio is similar to that found in the GC clouds, as expected if alcohols are also ejected from icy grain mantles by shocks in this galaxy(Charnley et al. 1995).

Table 5: Limits to the detection of C₂H₅OH

ν (MHz)	E _u (cm ⁻¹)	rms ^a (mK)	$\int T_{\text{MB}} dv$ ^b (K km s ⁻¹)
129665.7	16.6	3.0	< 1.440
131103.0	16.6	1.8	< 0.864
131502.7	20.1	C ₂ S	
132935.1	6.9	baseline	
133323.4	16.5	CH ₂ NH	
142285.0	25.8	1.8	< 0.864
144734.0	9.3	C ³⁴ S	
147427.4	21.0	2.9	< 1.392
152656.8	9.3	3.4	< 1.632
159781.8	12.2	NH ₂ CN	
160699.0	31.4	i=H ₂ S	
161609.0	26.1	NS	
173391.3	12.2	3.6	< 1.728
174232.9	15.7	c-C ₃ H	

^arms computed for 20 km s⁻¹ wide channels. If the transition is blended, the species is indicated.

^b3 σ limit to the integrated intensity assuming an emission width of 150 km s⁻¹.

4.4. The nuclear environment in NGC 253

The detection of new molecules in the extragalactic ISM, far from being a mere census of known species, provides a complete description of the chemical complexity within the nuclear environment of galaxies and a tool to establish the origin of this rich chemistry and the heating of the molecular gas.

In the following subsections we will compare the observed abundances in NGC 253 with those available for five external galaxies (Sect. 4.4.1) and five prototypical sources within the Milky Way (Sect. 4.4.2). The comparison focuses mainly on the abundance ratios between the different molecular species compared to those observed toward NGC 253. This will minimize the systematic error in the absolute fractional abundances due to the H_2 column density determinations. The relative abundances between molecules will provide us with a reliable chemical differentiation giving us insights into the dominant chemical mechanism acting in each source.

4.4.1. Comparison with other galaxies

We have selected the nearby galaxies NGC 4945, M 82 and IC 342 where most of the known molecular species have also been observed, and Maffei2 and NGC 6946 for which fewer species have been detected.

Table 6 presents the integrated intensities of the $^{13}\text{CO } J = 2 - 1$ transition that has been used to estimate the H_2 source averaged column density. We used the conversion $N(\text{H}_2) = 3.3 \cdot 10^{20} \text{cm}^{-2} I(^{13}\text{CO}_{2-1})$ (Mauersberger et al. 2003).

Table 6: Molecular hydrogen source averaged column density

Source	Transition $J - J'$	$\int T_{\text{MB}} dv$ K km s ⁻¹	θ_{beam} ($''$)	N_{H_2} cm ⁻²
NGC 253	¹³ CO 2 – 1	52.4 ^a	34	6.7 10 ²²
NGC 4945	¹³ CO 2 – 1	81.2 ^b	23	6.4 10 ²²
M 82	¹³ CO 2 – 1	29.4 ^a	34	3.8 10 ²²
IC 342	¹³ CO 2 – 1	17.2 ^a	34	2.2 10 ²²
Maffei 2	¹³ CO 2 – 1	13.9 ^a	34	1.8 10 ²²
NGC 6946	¹³ CO 2 – 1	22.2 ^c	21	1.5 10 ²²

Note. — A 20 $''$ source size was assumed for all targets.

^a10 m HHT by Mauersberger et al. (2003).

^b15 m SEST by Wang et al. (2004).

^c30 m IRAM by Israel & Baas (2001).

Table 7 shows the derived fractional abundances relative to H_2 towards the selected galaxies. Because of the frequency coverage of our survey, not all the species listed in Table 3 could be measured. Therefore, in Table 7, we have also included data of additional key molecular species from other studies, namely NH_3 , N_2H^+ and CN . H_2 and CO are not included as they are tracers of the total mass of the molecular material content. Species such as OH and H_2O have also been detected towards NGC 253 and many other galaxies. However, H_2O exhibits maser emission that does not allow us to determine directly the column densities, while OH shows extremely complex behavior involving a mixture of absorption, thermal and maser emission (e.g. Turner 1985; Ho et al. 1987; Frayer et al. 1998; Bradford et al. 1999; Henkel et al. 2004; Goicoechea et al. 2005). Unfortunately, there is not enough data available on CH , CH^+ , HCO , CO^+ and HOC^+ for this comparison.

In order to achieve the highest homogeneity in the derived abundances, we have collected all the line profile parameters from the available observations in the literature. From these values we have made our own estimates of the column densities for each molecule and each source with the assumptions used for NGC 253.

We have assumed a source size $\theta_s = 20''$ for *all* these sources (see e.g. Sect. 3.3 for NGC 253 and Wang et al. 2004 for NGC 4945). This is a fairly simple assumption for some of the targets and may lead to considerable errors in the column density determination. As this factor is also included in the source averaged column density determination of the molecular hydrogen, the error in the resulting fractional abundance will, however, cancel out to first order.

The top panel in Fig. 7 shows a graphical representation of the data in Table 7. Molecular species are ordered based on increasing abundances in NGC 253. We have also considered the logarithmic difference of abundances in each selected galaxy with respect to the abundances derived in this work for NGC 253 as $\Delta X = \log_{10}(X/X_{\text{NGC253}})$. This variable, ΔX , is plotted in the bottom panel of Fig. 7. The difference in the Y-axis between two species provides a measure of their abundance ratio relative to that in NGC 253.

M 82 shows relative abundances quite similar to those of NGC 253 in many but not all of the observed species. Evident chemical differences between both nuclear starbursts were already analyzed (Mauersberger & Henkel 1993; Takano et al. 1995, 2002; Wang et al. 2004), and have been interpreted as a difference in the evolutionary stage of both starbursts. Compared to that in NGC 253, the nuclear starburst in *M 82* represents an evolved state where PDRs dominate the heating of the molecular material (García-Burillo et al. 2002). From our comparison, the high relative abundance of C_3H_2 , a common PDR tracer, is particularly outstanding. On the other hand we note remarkably low abundances of CH_3OH and SiO , which are thought to be ejected from grain mantles into the gas-phase (Charnley et al.

1995; Martín-Pintado et al. 1992; Requena-Torres et al. 2005). This suggests that shocks do not play the dominant role within the nuclear region of M 82. Molecules such as HNCO, apparently associated with shock chemistry (Zinchenko et al. 2000), also show low relative abundances compared to those in NGC 253. Furthermore, the nuclear environment of M 82 is characterized by systematically lower relative abundances of CH_3CN , NH_3 and N_2H^+ . It is also interesting to note how other species used as PDR tracers, namely C^{34}S and C_2H (Meier & Turner 2005), do not show high relative abundances in M 82 compared to the other observed species. Moreover, they are a factor of $\sim 2 - 3$ less abundant than most other the species. If we compare the M 82 relative abundances with those of the Orion Bar in Sect. 4.4.2, we find that all the species with low abundances in M 82 show the same behavior in the Orion Bar. This comparison strongly supports the idea of M 82 as an evolved nuclear starburst largely dominated by PDRs.

In *NGC 4945*, relative abundances of all the detected molecular species resemble within a factor of 3 those of NGC 253. The non-detection of SiO indicates a clear underabundance, similar to what is seen towards M 82. On the other hand, unlike in M 82, CH_3OH shows an abundance similar to that in NGC 253. This resemblance between the abundances in NGC 4945 and NGC 253, altogether with excitation considerations and a detailed study of species such as CN, HCN, and HNC, has been interpreted as an intermediate evolutionary state, between NGC 253 and M 82 (Wang et al. 2004). From our comparison, the nuclear starburst of NGC 4945 shows much closer resemblance to NGC 253 than to M 82.

IC 342 shows high relative abundances of HC_3N and H^{13}CO^+ , while molecules such as C_2H and N_2H^+ have lower abundances as compared with NGC 253. Many of the available observations for IC 342 (marked by an asterisk in Table 7) were obtained near the D position as labeled by Downes et al. (1992), $\sim 15''$ north of the main nuclear star formation region. The abundance of C_2H given in Table 7 has been taken from Meier & Turner (2005) towards the D position. Its relative abundance is low compared to that in NGC 253. Even taking the C_2H abundance at the position where this molecule peaks (i.e. a value an order of magnitude higher towards the central position, Meier & Turner 2005), the relative abundances of this species with respect to the rest of molecules would be similar to that in NGC 253. High resolution maps from Meier & Turner (2005) clearly differentiate a region dominated by UV radiation from the central nuclear cluster and the region where the chemistry is dominated by shocks produced by collisions of clouds in a barred potential. Given the position towards which many of the spectra were taken, away from the dynamical center, the molecular emission of IC 342 should resemble more that of NGC 253 than that of M 82. In fact IC 342 does not show the relatively low HNCO abundance seen in M 82 but does show a similar low relative abundance of C_2H . Still, there is a large number of molecules not yet observed which are critical to fully evaluate the chemistry of IC 342, such as SiO, SO, OCS and CH_3OH .

As far as *Maffei 2* and *NGC 6946* are concerned, the available molecular information is not sufficient to establish a clear chemical differentiation from the other sources. What can be noted is a remarkably high relative abundance of HNC in Maffei 2 compared to the other galaxies and a low relative abundance of H₂CO in NGC 6946. Both galaxies also show low relative abundances of N₂H⁺.

Table 7: Molecular fractional abundances toward NGC 253 and other galaxies

Molecule	NGC 253	NGC 4945	M 82	IC 342	Maffei2	NGC 6946
HN ¹³ C	−10.6	−9.5	−9.5
H ¹³ CO ⁺	−10.4	−10.0	−9.9	−9.5*
H ¹³ CN	−9.9	−9.7	< −9.9	< −9.4*
SiO	−9.9	< −9.9	< −9.9	< −9.3*	< −9.1	...
CH ₃ CN	−9.5	...	< −9.7
C ³⁴ S	−9.4	−9.4	−9.3	−9.5*	...	< −9.0
c-C ₃ H ₂	−9.3	−8.9	−8.1
HC ₃ N	−9.2	−8.8	−8.7	−8.6
N ₂ H ⁺	−9.2	−9.2	−9.4	−9.6*	−9.7	−9.6
HNC	−9.0	−8.6	−8.8	−8.7	−8.7	−8.8
SO	−8.9	−8.7	< −8.5	< −8.7
HCO ⁺	−8.8	−8.4	−8.4	−8.8	−8.6	−8.5
HNCO	−8.8	−8.4	< −8.8	−8.6	−8.3	...
H ₂ CO	−8.6	−8.1	−8.2	−9.4	−8.8	−9.1
OCS	−8.4	< −7.5	−7.9	< −8.6
CN	−8.3	−7.7	−8.2	−8.3*
HCN	−8.3	−8.3	−8.4	−8.5*	−8.3	−8.5
CS	−8.2	−8.4	−8.2	−8.4*	−8.7	−8.7
CH ₃ CCH	−8.2	−8.0	−7.7
CH ₃ OH	−7.9	−7.4	< −8.3	< −7.8	−7.7	−7.9
C ₂ H	−7.7	−7.3	−7.6	< −8.4
NH ₃	−7.2	...	−8.4	−7.3	−7.1	...

*Observations taken $\sim 15''$ away from the central position (see Sect. 4.4.1 for details).

References. — NGC 253, this paper, Martín et al. (2003)[NS,NO], Martín et al. (2005)[OCS], Mauersberger et al. (2003)[NH₃], Henkel et al. (1988)[CN], Mauersberger & Henkel (1991)[N₂H⁺]; NGC 4945, Wang et al. (2004), Henkel et al. (1994)[SiO]; M 82, Mauersberger & Henkel (1989)[CS,C³⁴S], Mauersberger & Henkel (1991)[N₂H⁺,SiO,H¹³CO⁺], Mauersberger et al. (1991)[C₃H₂,CH₃CN,CH₃CCH], Mauersberger et al. (1995)[OCS], Hüttemeister et al. (1997)[H₂CO,CH₃OH], Henkel et al. (1988)[CN,HC₃N,C₂H], Henkel et al. (1998)[HCO⁺,HCN,H¹³CN], Petuchowski & Bennett (1992)[SO], Nguyen-Q-Rieu et al. (1991)[HNCO], Nguyen-Q-Rieu et al. (1992)[HCN,HCO⁺,H¹³CO⁺], Wild (1990)[HCN,HCO⁺], Weiß et al. (2001)[NH₃],Hüttemeister et al. (1995)[HNC]; IC 342, Mauersberger & Henkel (1989)[CS], Mauersberger & Henkel (1991)[N₂H⁺,SiO,H¹³CO⁺], Mauersberger et al. (1995)[C³⁴S,OCS,HC₃N,H₂CO], Henkel et al. (1988)[CN,HNC,HC₃N], Hüttemeister et al. (1995)[HNC], Hüttemeister et al. (1997)[H₂CO,CH₃OH], Petuchowski & Bennett (1992)[SO], Wild (1990)[HCN,HCO⁺], Nguyen-Q-Rieu et al. (1991)[HNCO], Nguyen-Q-Rieu et al. (1992)[HCN,HCO⁺,H¹³CO⁺], Henkel et al. (1998)[HCN, H¹³CN], Meier & Turner (2005)[C₂H], Mauersberger et al. (2003)[NH₃]; Maffei2, Mauersberger & Henkel (1989)[CS], Mauersberger & Henkel (1991)[SiO,N₂H⁺], Hüttemeister et al. (1997)[H₂CO,CH₃OH], Nguyen-Q-Rieu et al. (1991)[HNCO], Nguyen-Q-Rieu et al. (1992)[HCO⁺,HCN], Henkel et al. (2000); Mauersberger et al. (2003)[NH₃]; NGC 6946, Hüttemeister et al. (1997)[H₂CO, CH₃OH], Mauersberger & Henkel (1989)[CS, C³⁴S], Nguyen-Q-Rieu et al. (1992)[HCO⁺, HCN], Mauersberger & Henkel (1991)[N₂H⁺].

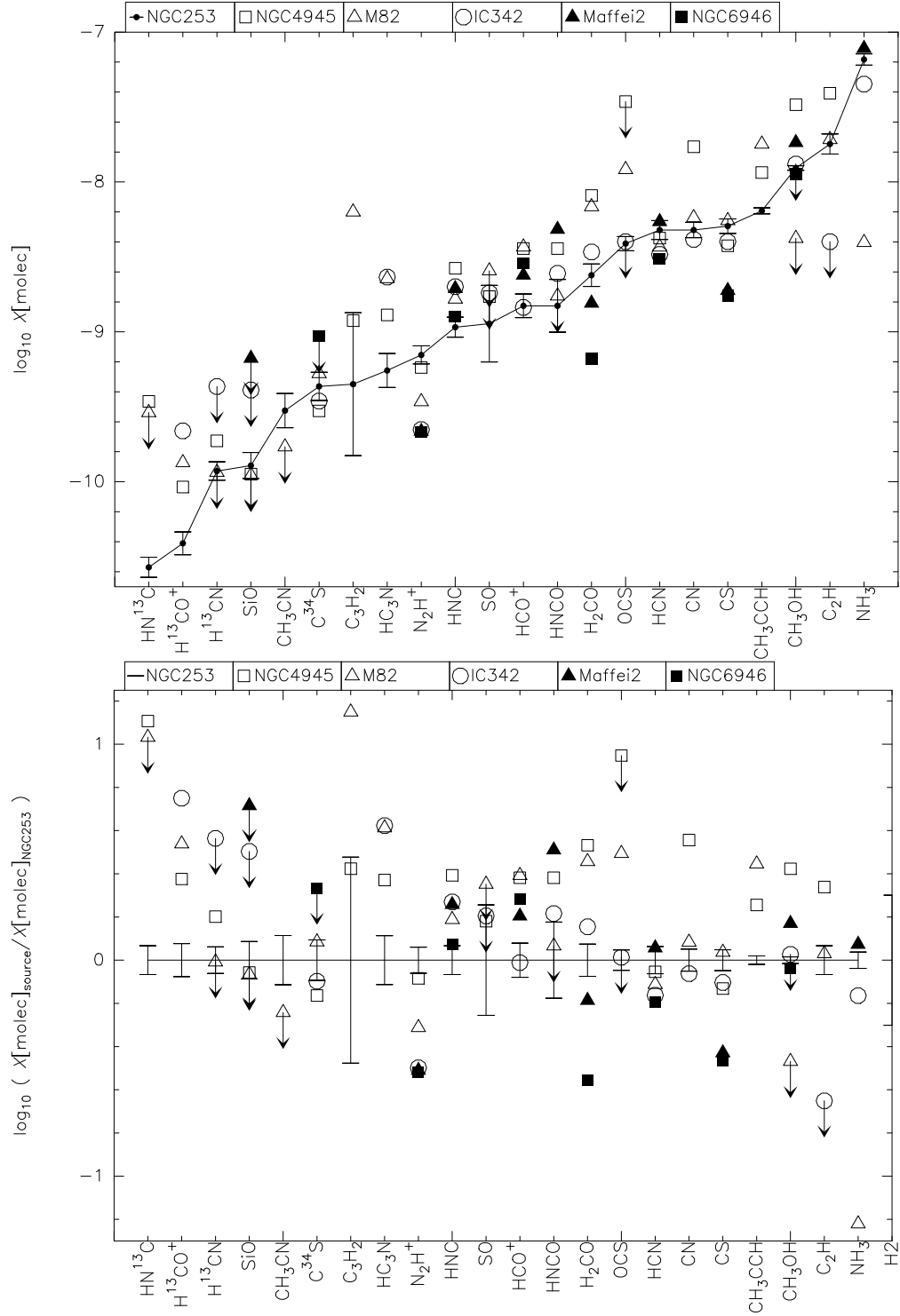


Fig. 7.— Molecular abundances (X) of selected extragalactic sources compared to those of NGC253. Arrows represent upper limits. A continuous line connects the abundances in NGC253. *Top panel:* Logarithmic fractional abundances relative to H_2 as presented in Table 7. *Bottom panel:* Logarithmic abundances for each species normalized to that measured in NGC253.

In order to quantify this comparison, Table 8 shows the mean and rms of ΔX for each source for two cases. The first only uses the species detected in both sources. The number of molecules included in the calculations is also indicated. The second also uses upper limits to the abundances derived for the comparison sources. To take these limits into account, we followed two criteria: upper limits higher than the abundances measured towards NGC 253 were rejected as they do not provide useful information for the comparison; for the calculations, the other observed limits, lower than the abundances in NGC 253, where divided by two as an estimated true value. The second assumption may overestimate some abundances, but any other constraint might result in biased guesses. While the mean value, $\overline{\Delta X}$, only gives an the overall absolute difference in the abundances of each source as compared with NGC 253, the rms of ΔX provides us with a fairly reliable measurement of differences in the abundance pattern that defines the chemistry of each object. M 82, as pointed out before, clearly differs chemically from NGC 253, showing the highest rms values. NGC 4945 and IC 342 are much closer to NGC 253.

Table 8: Statistical comparison of abundances of selected galaxies with those in NGC 253.

Source	Without limits			With limits		
	$\overline{\Delta X}$	$\text{rms}(\Delta X)$	num.	$\overline{\Delta X}$	$\text{rms}(\Delta X)$	num.
NGC 4945	0.30	0.29	18	0.27	0.32	19
M 82	0.19	0.51	15	0.05	0.54	19
IC 342	0.08	0.34	12	0.00	0.42	13
Maffei 2	0.02	0.31	9	0.02	0.31	9
NGC 6946	-0.20	0.30	7	-0.20	0.30	7

Note. — $\Delta X = \log_{10} (X/X_{\text{NGC 253}})$. See last paragraph in Sect. 4.4.1 for details.

4.4.2. Comparison with prototype Galactic sources

We have selected five Galactic sources, namely Sgr B2(N), Sgr B2(OH), TMC-1, L134N, and the Orion Bar, which are considered to be prototypes of their respective chemistry within the Galaxy. All these sources have been the target of multi-transition studies and some of them of frequency surveys. Table 9 shows the abundances of all the molecules observed in the NGC 253 survey compared to those of these Galactic sources. In order to achieve consistency among ratios, we have tried, when available, to use values from line surveys or multi-line studies for each source.

In the same way as in the extragalactic comparison, the top panel in Fig. 8 shows a graphical representation of the data in Table 9, where molecular species are ordered based on increasing NGC 253 abundances. The bottom panel in Fig. 8 shows the logarithmic abundance of each molecule normalized to the abundance measured in NGC 253.

Sgr B2(N) is believed to represent the prototype of a *hot molecular core chemistry* associated with massive star formation near the nucleus of the Milky Way. A large number of molecular species have been identified towards this source which is the brightest molecular line emitter within the Galaxy (Friedel et al. 2004, and references therein). There are clear differences between the abundances found towards Sgr B2(N) and those in NGC 253. A set of molecules, namely CH₃CN, HC₃N, NS, H₂CS, SO₂, CH₂NH, SO, CH₃OH and NO, show abundances relative to the other species $\sim 2 - 3$ orders of magnitude larger than what we observe towards NGC 253. Almost all the other species observed towards Sgr B2(N) have smaller abundances than in NGC 253, but their relative abundances are, within an order of magnitude, similar to those in NGC 253. Exceptions are HOCO⁺ and C₂H that show lower relative abundances by factors ~ 30 and 100 , respectively, in the Sgr B2(N) hot core. Moreover, the rotation temperatures derived from the observed molecules in NGC 253 are low compared to the typical temperatures of > 70 K observed towards hot cores. Even if hot cores associated with massive protostars are present in the nuclear environment of NGC 253, they clearly do not dominate the molecular emission. While the angular size of the Sgr B2 molecular cloud complex is $\sim 18'$ (Scoville et al. 1975), the emission of some large complex molecules towards Sgr B2(N) appears concentrated within a region of $\sim 5''$, corresponding to 0.2 pc at a distance of 8.5 kpc (Kerr, F.J. & Lynden-Bell, D. 1986). At the distance of NGC 253, such a source would have a diameter of $< 0''.02$, and because of beam dilution, its detection is certainly out of reach for the 30 m telescope. A large number of such sources would be needed in order to be able to observe traces of their complex chemistry.

The Orion Bar has been selected as the prototype of *photodissociation regions* (PDRs). A large fraction of the molecular gas in the Milky Way and in external galaxies is expected to be affected by PDRs (Hollenbach & Tielens 1997). In PDRs, molecular emission originates

from the surface layers of interstellar molecular clouds exposed to intense far-ultraviolet photons from nearby young OB stars. The non-detection of molecules such as CH_3CN and HNCO towards the Orion PDR clearly indicates a low relative abundance of these species with respect to other molecules, which is in contrast with the observed NGC 253 abundances. Similarly, the relative abundances of SiO , SO_2 , CH_3OH , C_2H and NO appear to be $\sim 1 - 2$ orders of magnitude lower in the Orion bar than in NGC 253. High abundances of hydrocarbon radicals, such as C_2H and C_3H_2 , are observed towards PDRs (Fossé et al. 2000; Fuente et al. 1993, 2003; Pety et al. 2005). In this context, it is surprising to see how C_2H and C_3H_2 , commonly used as PDR tracers, show relatively low abundances in the Orion PDR when compared not only with NGC 253 but also with the prototypical Galactic sources except the Sgr B2(N) hot core. The observations of the Orion Bar have been taken from the position of maximum H_2 column density (Jansen et al. 1995; Fuente et al. 1996), which does not match the position of highest C_3H_2 abundance (Fuente et al. 2003). However, the contribution of the position of the C_3H_2 emission peak to the total column density is smaller than that of the H_2 column density peak. Therefore, it is expected that the molecular abundance of the H_2 peak dominates the emission of PDRs, also in external galaxies. Anyhow, even if we consider the position of the larger C_3H_2 abundance (up to one order of magnitude, Fuente et al. 2003), the relative abundance would still be close to that found in NGC 253. From this comparison as well as that to M 82 (see Sect. 4.4.1) it is clear that the chemistry of the nuclear environment of NGC 253 is not dominated by photodissociation.

Quiescent cold dark clouds are represented by *TMC-1* and *L134N*. The molecular composition at sites of low mass star formation is dominated by gas-phase ion-molecule chemistry due to a lack of embedded luminous sources. In our comparison, both dark cloud complexes have in common low relative abundances of SiO and, to a lesser degree, of CH_3OH . The remaining species behave quite differently in each source. SO_2 , H_2S , HNCO and NO , show low abundances in TMC-1 while C_2S and C_3H_2 appear to have abundances larger than in NGC 253 by up to one order of magnitude. On the other hand, L134N shows a high SO abundance and relatively low abundances of HC_3N and CH_3CCH . The abundance pattern defined by these two dark clouds clearly does not follow the relative abundances found towards NGC 253. In addition, even the rotation temperatures derived for NGC 253, which in general are smaller than T_{kin} , are higher than the typical kinetic temperature ($T_{\text{kin}} \sim 10\text{ K}$) measured towards dark clouds.

Sgr B2(OH), located at the southern end of the Sgr B2 molecular envelope, is free from the emission stemming from the hot cores in this cloud. This position in the Sgr B giant molecular cloud is taken as the prototype of *Galactic center (GC) molecular cloud complexes* (Martín-Pintado et al. 1997). The H_2 column density of this source has been estimated to be

roughly $N(\text{H}_2) = 5 \cdot 10^{23}$ (Nummelin et al. 2000). The relative abundances of all the species measured towards this Galactic center molecular cloud complex appear to closely follow the abundance pattern in NGC 253 within a factor ~ 5 . The only species clearly underabundant in Sgr B2(OH) when compared to NGC 253 is $\text{c-C}_3\text{H}$ but this molecule is only tentatively detected towards NGC 253. Thus, the ratios between any of the observed species are similar to those in NGC 253 within one order of magnitude.

Table 9: Comparison of NGC 253 fractional molecular abundances with those in selected Galactic sources

Molecule	NGC 253	Sgr B2(N)	Sgr B2(OH)	TMC-1	L134N	Orion Bar
HN ¹³ C	−10.6	−11.0
H ¹³ CO ⁺	−10.4	−11.4	−10.3
SiO	−9.9	−10.7	...	< −11.6	< −11.4	−10.3
NH ₂ CN	−9.7	−10.1	−10.0
C ₂ S	−9.7	...	−9.6	−8.1	−9.2	...
CH ₃ CN	−9.5	−6.7	−9.4	−9.0	< −9.0	< −10.3
c-C ₃ H	−9.5	−10.5	< −10.9	−9.3
HOCO ⁺	−9.4	−10.5	−9.7
C ³⁴ S	−9.4	−10.2	−9.0
c-C ₃ H ₂	−9.3	−10.5	−9.8	−8.0	−8.7	−9.7
HC ₃ N	−9.2	−7.5	−9.0	−8.2	−9.7	...
NS	−9.2	−7.0	...	−9.1	−9.5	...
H ₂ CS	−9.2	−6.8	−8.7	−8.5	−9.2	...
SO ₂	−9.1	−6.6	−8.7	< −9.0	−8.4	−9.9
CH ₂ NH	−9.1	−7.0	−9.2
H ₂ S	−9.1	−9.9	...	< −9.3	−9.1	−8.2
HNC	−9.0	−7.7	−8.2	−9.0
SO	−8.9	−6.9	−8.7	−8.3	−7.7	−8.0
HCO ⁺	−8.8	−8.1	−8.1	−8.5
HNCO	−8.8	−9.2	−8.4	−9.7	...	< −10.8
H ₂ CO	−8.6	−9.3	−8.6	−7.7	−7.7	−8.2
OCS	−8.4	−8.6	−8.3	−8.7	−8.7	...
HCN	−8.3	−7.7	−8.4	−8.3
CS	−8.2	−8.0	−9.0	−7.6
CH ₃ CCH	−8.2	−8.4	−8.8	−8.2	< −8.9	...
CH ₃ OH	−7.9	−5.8	−7.3	−8.7	−8.5	−9.0
C ₂ H	−7.7	−9.7	...	−7.1	< −7.3	−8.7
NO	−7.2	−6.0	...	< −7.5	−7.2	−8.6

References. — *NGC 253*: this paper and Martín et al. (2003)[NS,NO], Martín et al. (2005)[OCS];
Sgr B2N: Nummelin et al. (2000) and Minh et al. (1991)[H₂S]. $N(\text{H}_2) = 3.0 \times 10^{24} \text{ cm}^{-2}$ from Nummelin et al. (2000);
Sgr B2(OH): Cummins et al. (1986) and Turner (1991). $N(\text{H}_2) = 5 \times 10^{23} \text{ cm}^{-2}$ (see text for details on this estimate);
TMC-1 and L134N: Ohishi et al. (1992), McGonagle et al. (1994)[NS], Ziurys et al. (1989)[SiO]. $N(\text{H}_2) = 1.0 \times 10^{22} \text{ cm}^{-2}$ from Ohishi et al. (1992);
Orion Bar: Jansen et al. (1995), Fuente et al. (2003)[C₃H₂], Schilke et al. (2001)[SiO]; $N(\text{H}_2) = 6.5 \times 10^{22} \text{ cm}^{-2}$ from Jansen et al. (1995).

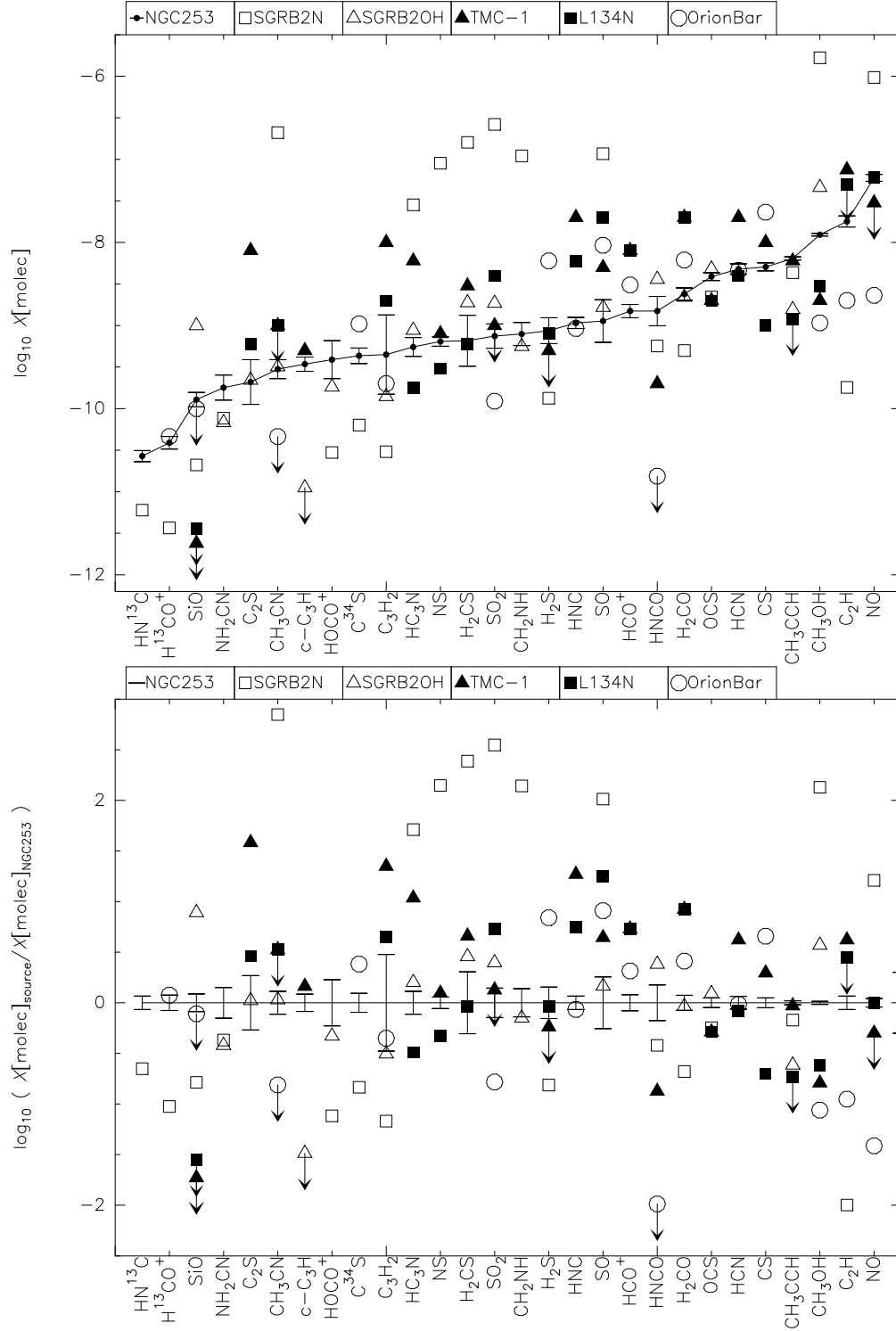


Fig. 8.— Molecular abundances (X) of selected Galactic sources compared to those of NGC253. Arrows represent upper limits. A continuous line connects the abundances in NGC253. *Top panel:* Logarithmic fractional abundances relative to H_2 as shown in Table 9. *Bottom panel:* Logarithmic abundances for each species normalized to that measured in NGC253.

In analogy to our statistical comparison of molecular abundances in prototypical nearby galaxies shown in Table 8, Table 10 presents a comparison between NGC 253 and the selected Galactic sources. To calculate the parameters, the available abundances in Table 9 have been taken into account following the criteria explained at the end of Sect. 4.4.1. Given the uncertainty of its detection, $\text{c-C}_3\text{H}$ was not included. The computed rms of the logarithmic differences shows the envelope of the Sgr B2 complex as the one most closely resembling NGC 253.

Table 10: Statistical comparison of abundances of selected Galactic sources with those in NGC 253.

Source	Without limits			With limits		
	$\overline{\Delta X}$	rms(ΔX)	num.	$\overline{\Delta X}$	rms(ΔX)	num.
Sgr B2(N)	0.40	1.50	22	0.40	1.50	22
Sgr B2(OH)	0.07	0.40	16	-0.04	0.58	17
TMC-1	0.47	0.66	18	0.26	0.85	21
L134N	0.18	0.58	16	-0.00	0.76	18
OrionBar	-0.07	0.71	14	-0.28	0.85	17

Note. — See Table 8 and Sect. 4.4.2 for details.

The agreement in relative abundances between NGC 253 and a typical Galactic center cloud is a remarkable and clear indication that the heating and chemistry of the bulk of the ISM is dominated by the same processes.

The molecular envelope around the star forming region Sgr B2 is formed by a relatively dense and warm material ($n_{\text{H}_2} = 2 \times 10^5 \text{ cm}^{-3}$ and $T_{\text{kin}} = 40\text{--}60 \text{ K}$, de Vicente et al. 1997). The large abundances of NH_3 , SiO and $\text{C}_2\text{H}_5\text{OH}$ observed in the gas phase of the Galactic center molecular clouds are claimed to be the result of grain chemistry and subsequent ejection onto the gas phase due to the disruption of grains by low velocity shocks ($v < 20 \text{ km s}^{-1}$, Flower et al. 1995; Martín-Pintado et al. 1997, 2001). In the Galactic center, the possible origin for these shocks is so far unclear. It has been claimed that they could be produced by the large-scale shocks associated with cloud-cloud collisions due to the orbital motion of molecular clouds in a barred potential (Hasegawa et al. 1994; Sato et al. 2000) and the interaction of expanding bubbles due to supernova events and/or strong stellar winds from Wolf-Rayet stars (Sofue 1990; de Vicente et al. 1997; Martín-Pintado et al. 1999) associated with a burst of star formation that occurred 10^7 years ago (Rodríguez-Fernández et al. 2004; Rodríguez-Fernández & Martín-Pintado 2005).

5. Conclusions

1. We present the first unbiased molecular line survey of an extragalactic source. The survey covers the 2 mm atmospheric window from 129.1 to 175.2 GHz toward the inner 200 pc of NGC 253. A total of 111 features are identified as transitions of 25 different molecular species, eight out of which (three tentatively) have been detected for the first time outside the Milky Way. The rare isotopes, ^{34}SO and HC^{18}O^+ , were also detected for the first time in an extragalactic source. Additionally, three hydrogen recombination lines and, tentatively, two deuterated species are identified, N_2D^+ and DNC . The origin of the observed features of both N_2D^+ and DNC is still unclear and deserves further investigation. If real, these would represent the first deuterated molecules observed beyond the Magellanic Clouds. Column densities and rotation temperatures have been determined for each species under Local Thermodynamic Equilibrium (LTE) conditions.
2. As a result of this survey and by adding existing data from three molecules, namely NH_3 , N_2H^+ and CN , we obtain the most complete description to date of the chemical complexity within the nuclear few hundred parsecs of a starburst galaxy. We have performed a comparison between the chemistry of NGC 253 and those of five other outstanding nearby galaxies. This comparison clearly shows the strong chemi-

cal differentiation between nuclei of galaxies. Most prominent differences are observed between NGC 253 and M 82. This can be interpreted in terms of a more evolved stage of the nuclear starburst in M 82. The chemistry of NGC 4945, though claimed to be at an intermediate stage of evolution between NGC 253 and M 82, clearly resembles more that of NGC 253 except for the lack of SiO. Similarly, the position within the nuclear region of IC 342, where most of the molecular observations have been made, show relative abundances close to those in NGC 253. This position is far from the main region of star formation where PDRs are claimed to dominate the chemistry.

As far as Maffei2 and NGC 6946 are concerned, the available molecular observations do not yet allow us to carry out a similarly detailed comparison.

3. A comparison of the molecular abundances of NGC 253 with selected Galactic sources shows a striking similarity between NGC 253 and Sgr B2(OH). The latter source, located in the envelope of Sgr B2, is commonly taken as the prototype of the molecular cloud complexes in the Galactic center region. This indicates that the chemistry of the nuclear molecular environment in NGC 253 and the Galactic center molecular clouds are driven by similar chemical processes. If this is the case, the chemistry and the heating of the nuclear molecular material in NGC 253 is dominated by large-scale low velocity shocks.
4. The comparison with Galactic sources also shows a close similarity between the abundances within the nuclear starburst of M 82 and those of the Orion Bar, the prototype of a photon dominated region. This resemblance fully supports the idea of the chemistry in M 82 being dominated by PDRs.

SM and RM were supported by the *Programas de Acciones Integradas* between Spain and Germany. JMP has been partially supported by the Spanish Ministerio de Educación y Ciencia under projects ESP 2004-00665, AYA 2002-10113-E and AYA 2003-02785-E. SGB acknowledges financial support from AYA 2003-07584 and ESP 2003-04957. We would like to thank the referee, whose comments helped to significantly improve the paper.

A. Gaussian fitting to blended lines

Table 1 includes a label in the third column indicating if and how the respective spectral feature is affected by blending. In the following the encountered different cases are described:

- $b \rightarrow \text{blended}$: Some observed features are composed of several transitions from different species. If the line is only partially blended, it is still possible to separate the individual components by fitting different Gaussian profiles. For these fits, sometimes it was necessary to fix the velocity and/or linewidth.
- $s \rightarrow \text{synthetic}$: The blending may prevent us from making a reliable multiple Gaussian fitting to an observed feature. In this case, when we have observed several transitions of one of the species contributing to the blended feature, it is possible to use these to estimate the species' contribution to the blended feature by interpolating or extrapolating the linear fit to the rotation diagrams (see Appendix B.1). This is equivalent to using Eq. B6 to estimate the expected integrated intensity of a line from the derived column density and rotation temperature. Using the estimated line intensity and the linewidth and radial velocity of the other observed transitions we subtract the expected synthetic Gaussian profile from the spectrum. The estimated integrated line intensities using this method have been plotted in the corresponding rotation diagrams with open symbols (Fig. 5). The transitions from other species contributing to the blended feature have been fitted to the residual spectrum after the subtraction of the synthetic profile.
- $hf \rightarrow \text{hyperfine}$: Some species show transitions which consist of a group of unresolved hyperfine components. The relative intensities of these lines are fixed by their spectroscopic parameters, assuming LTE and optically thin line emission. Thus, the fitting has been carried out with a comb of Gaussian profiles at the rest frequencies of the hyperfine components with the same widths and with fixed line intensities relative to the main component which is taken as a free parameter. The derived parameters shown in Table 1 correspond to the integrated intensity of all the hyperfine components but the frequency, line intensity and velocity refers to the main hyperfine component.
- $m \rightarrow \text{multi-transition}$: Some features of species such as CH_3OH and CH_3CN consist of groups of overlapping transitions, involving different energy levels. In these cases, a single Gaussian profile has been fitted to the observed spectral feature. The total integrated line intensity of all the blended transitions has been used to derive rotation diagrams as described in Appendix B.2.

B. Rotation Diagrams

B.1. Basics

Assuming optically thin emission for the observed molecular transitions, the column density in the upper level can be derived as

$$N_u = \frac{8\pi k\nu^2}{hc^3 A_{ul}} \left(1 - \frac{J_\nu(T_{\text{BG}})}{J_\nu(T_{\text{ex}})} \right)^{-1} \int T_{\text{B}} dv, \quad (\text{B1})$$

where A_{ul} , the Einstein coefficient for a transition connecting the levels u and l , can be written as $A_{ul} = (64\pi^4\nu^3/3hc^3)S\mu_{ul}^2/g_u$, and $J_\nu(T) = (h\nu/k)[\exp(h\nu/kT) - 1]^{-1}$, with T_{BG} denoting the temperature of the background, T_{ex} the excitation temperature of the transition and g_u the degeneracy of the upper level.

In the Rayleigh-Jeans approximation ($h\nu \ll kT$), and assuming $T_{\text{ex}} \gg T_{\text{BG}}$, eq. B1 can be reduced to

$$N_u = \frac{8\pi k\nu^2}{hc^3 A_{ul}} W, \quad (\text{B2})$$

where the integrated brightness temperature $\int T_{\text{B}} dv$ is denoted as W . If LTE is assumed, the population distribution of all the levels can be represented by a single temperature, the rotation temperature (T_{rot}), given by

$$\frac{N_u}{g_u} = \frac{N}{Z} e^{-E_u/kT_{\text{rot}}}, \quad (\text{B3})$$

where N is the total column density, E_u is the energy of the upper level, and Z the partition function calculated as

$$Z = \sum_{\forall i} g_i e^{-E_i/kT_{\text{rot}}}. \quad (\text{B4})$$

Using Eq. B2 in Eq. B3 we obtain

$$N = \frac{8\pi k\nu^2}{hc^3 A_{ul} g_u} W e^{E_u/kT_{\text{rot}}} \quad (\text{B5})$$

or the equivalent logarithmic expression

$$\log \frac{8\pi k\nu^2}{hc^3 A_{ul} g_u} W = \log \frac{N}{Z} - \frac{\log e E_u}{k T_{\text{rot}}}, \quad (\text{B6})$$

which constitutes the basic equation for the rotation diagrams (see Blake et al. 1987; Turner 1991; Goldsmith & Langer 1999, for a complete description of this method). Plotting N_u/g_u for each transition against the energy of its upper level in a logarithmic scale, the population distribution can be fitted by a straight line that provides the total column density divided by the partition function as well as T_{rot} .

B.2. Blended lines

Whenever a molecular feature is composed of a number of unresolved blended transitions of a given molecular species, rotation diagrams cannot be directly used to determine the physical properties of the molecular emission. The spectroscopic parameters of the blended individual transitions within an observed feature allow us to estimate the contribution of each transition to the total integrated intensity, assuming LTE and optically thin emission. Thus, using eq. B5 we can express the relative integrated intensity between two transition with Einstein coefficients A'_{ul} and A''_{ul} , energies of the upper level E'_u and E''_u , and degeneracies g'_u and g''_u as

$$\frac{W'}{W''} = \frac{\nu'^2 A'_{ul} g'_u}{\nu''^2 A''_{ul} g''_u} e^{(E''_u - E'_u)/k T_{\text{rot}}^0}. \quad (\text{B7})$$

This allows us to compute the relative intensity of transition for a given T_{rot}^0 . We will differentiate between the temperature, T_{rot}^0 , we assume for estimating the contribution of each transition to the blended line, and the rotational temperature, T_{rot} , derived from the rotation diagram.

If we consider the case of a molecule with hyperfine structure where all the transitions within a feature have the same upper level energy, then we can make the assumptions of $E'_u \approx E''_u$ and $\nu' \approx \nu''$. Therefore, the contribution of each transition will not depend on the assumed T_{rot} and will only depend on the spectroscopic parameters of each transition in the form

$$\left(\frac{W'}{W''} \right)_{\text{HF}} = \frac{A'_{ul} g'_u}{A''_{ul} g''_u}. \quad (\text{B8})$$

When the contribution of each hyperfine transition to the total line is computed and plotted on the rotation diagrams, they will all lie in the same point in the rotation diagram (see NO and NS diagrams).

In the general case where $E'_u \neq E''_u$, the calculated contribution of each line for a given T_{rot}^0 , will lie on a straight line when included into the rotation diagram. The line traced by these points will have the slope $\log_{10} e/k T_{\text{rot}}^0$.

The LTE approximation assumes that all the transitions will lie in a straight line in the rotation diagram, thus we can modify the assumed T_{rot}^0 used to calculate the contributions within the blended lines to obtain the best fit to a straight line to all data in the rotation diagram. At this point we will obtain the situation in which $T_{\text{rot}}^0 \approx T_{\text{rot}}$.

In this paper we have several examples where this method has been applied, i.e. the CH_3CN rotation diagram, where only two multiple-transition lines are plotted, the CH_3CCH diagram, where three blended lines are perfectly aligned to a straight line and the CH_3OH diagram, where a mixture of multi-transition lines and single lines are plotted altogether (Fig. 5).

We have to take special care when dealing with the symmetric top rotors such as CH_3CN and CH_3CCH . In this case, the rotation temperature is not sufficient to describe the relative population of the levels given that both T_{kin} and T_{rot} are required to evaluate the partition function as described by Turner (1991). Thus T_{rot} would characterize the population of J levels within a K ladder, while T_{kin} would describe the population between K -ladders. Our observations do not resolve the transitions of different K -ladders. We assume both temperatures to be the same ($T_{\text{kin}} = T_{\text{rot}}$) so that the population of all levels is described by a single rotation temperature. Given that T_{rot} is a lower limit to T_{kin} , with typically $T_{\text{rot}} \ll T_{\text{kin}}$, this assumption may result in an overestimation of the column density derived from rotation diagrams as the contribution to the total integrated intensity of the $K \geq 1$ levels may have been underestimated. On the other hand, the evaluation of the partition function will also be underestimated. Thus, the overall effect in the total column density determination is not expected to be more than a factor of 2 – 3 while the derived rotation temperature will only be marginally affected.

C. Notes on individual molecules

In the following, we will discuss the fitting procedure of the identified molecular species in detail.

C.1. Carbon monosulfide: CS

Only the $J = 3 - 2$ transition of carbon monosulfide at 147 GHz is observed in the survey. It appears to be partially contaminated by the H35 α recombination line. The estimated Gaussian profile derived from the observed H34 α (Sect. C.26) has been subtracted to account for its contribution.

Two rare isotopes, ^{13}CS and C^{34}S at 144.6 and 138.8 GHz respectively, are also observed in the spectral scan. Martín et al. (2005) used these observations of CS and its isotopes, as well as additional CS lines, to derive isotope ratios of $^{32}\text{S}/^{34}\text{S} \sim 8 \pm 2$ and $^{34}\text{S}/^{33}\text{S} > 9$. From the observation of additional CS transitions at 3, 1.5 and 1.2 mm, Martín et al. (2005) derive a $T_{\text{rot}} \sim 10$ K.

C.2. Nitric oxide: NO

One rotational transition of nitric oxide (150.2 and 150.5 GHz) has been identified in our survey. Martín et al. (2003) confirmed this identification by observing additional transitions at 250 GHz. These transitions have also been included in the rotation diagram in Fig. 5. The topology of the NO energy levels is similar to that of NS. Transitions connecting upper and lower levels are labeled Π^+ and Π^- .

It was only possible to fit the Π^+ hyperfine group of the transition at 150.2 GHz, given that the Π^- group is blended with the more intense H_2CO line (Sect. C.14). As shown in Table 1, the Π^- group of transitions has been estimated by fixing width and radial velocity of each component to the values derived from the fitting to the Π^+ transition and the line intensities determined by their relative line strengths.

C.3. Nitric sulfide: NS

One rotational transition of nitric sulfide (161.2 and 161.7 GHz) has been detected in our survey. Martín et al. (2003) confirmed the identification by detecting other transitions at 115 and 207 GHz. The rotation diagram in Fig. 5 includes these additional transitions.

This molecule presents Λ -doubling and hyperfine splitting. Because of the Λ -doubling, each rotational level is divided into two levels with opposite parity. Transitions connecting the upper levels are denoted as e and those connecting the lower levels as f (see Table 1). We are able to resolve the split rotational levels due to Λ -doubling but the intrinsic linewidths prevent us from resolving the hyperfine structure.

C.4. Sulfur monoxide: SO

We detect three transitions of sulfur monoxide (138.2, 159 and 172.2 GHz). The velocity components at 180 km s^{-1} and 275 km s^{-1} are clearly identified. As seen in the rotation

diagrams (Fig. 5), the 275 km s^{-1} component of the $3_4 - 2_3$ transition shows a much higher intensity than expected if we assume both components to have the same rotation temperature. This is likely due to the contamination of this component by the $8_{1,8} - 7_{1,7}$ transition of NH_2CN . The uncertainty in the contribution of this line due to the noise strongly affects the fitting of the high velocity component of this SO transition.

One of the isotopic substitutions of sulfur monoxide, ^{34}SO (135.8 GHz) is detected blended with a SO_2 transition. This faint feature has been fitted with a double Gaussian, with the velocity and width of each component fixed to the values derived from the same transition, $4_3 - 3_2$, of the main isotope. We calculate a ratio $^{32}\text{SO}/^{34}\text{SO} = 5.1 \pm 1.2$, using both velocity components of the $4_3 - 3_2$ transition of both isotopes. This ratio is consistent within the errors with $^{32}\text{S}/^{34}\text{S} = 8 \pm 2$ as derived by Martín et al. (2005) from CS data.

C.5. Silicon monoxide: SiO

Two transitions of silicon monoxide in the ground vibrational state are observed at 130.3 and 173.7 GHz ($J = 3 - 2$ and $J = 4 - 3$, respectively). It is possible to identify two velocity components from the $J = 3 - 2$ transition at 180 and 260 km s^{-1} . Velocity and width of the fainter and more noisy $J = 4 - 3$ transition were fixed to the values obtained from the fit to the $J = 3 - 2$ line. The rotation diagram has been derived for each velocity component (solid and dashed lines in Fig. 5).

C.6. Hydrogen sulfide: H_2S

Only one line of hydrogen sulfide at 168.8 GHz, with velocity components at 180 and 275 km s^{-1} , is detected in the 2 mm survey (see also Martín et al. 2005). Physical parameters in Table 2 have been derived by assuming a rotation temperature of 12 K similar to that derived for many other species (see Table 2).

C.7. Hydrocyanic acid: HCN

The $J = 2 - 1$ transition of HCN at 177.2 GHz lies outside the covered frequency range, but the $2 - 1$ line of its H^{13}CN isotope at 172.6 GHz was detected. A fit to this transition allows us to estimate the abundance of HCN if we assume a rotation temperature of 12 K and the $^{12}\text{C}/^{13}\text{C}$ ratio of 40 derived by Henkel et al. (1993).

C.8. Oxomethylum: HCO^+

The only 2 mm transition of the main species of oxomethylum, with energy levels low enough to be observable in the ISM of NGC 253, at a frequency of 178.3 GHz, lies a few GHz above the observed frequency range. Nevertheless, one of its isotopes, H^{13}CO^+ , has been detected in the $J = 2 - 1$ transition at 173.5 GHz, near the upper end of the spectral scan. Two velocity components can be fitted to the observed profile. The HCO^+ column density shown in Table 2 has been calculated from the integrated intensity of the measured H^{13}CO^+ line with an excitation temperature of 12 K and an isotopic ratio of $^{12}\text{C}/^{13}\text{C} \sim 40$ (Henkel et al. 1993).

The $J = 2 - 1$ transition of HC^{18}O^+ is also identified at 170.3 GHz. The low velocity component shows a higher intensity than expected from the observed H^{13}CO^+ profile as well as a slightly higher velocity. If we compare both profiles we derive a $\text{H}^{13}\text{CO}^+/\text{HC}^{18}\text{O}^+$ ratio of 1.7 ± 1.1 and 2.9 ± 1.2 for the low and high velocity components, respectively. The value derived for the high velocity component agrees within the errors with the expected value of ~ 3.7 if we assume the isotopic ratios $^{12}\text{C}/^{13}\text{C} = 40$ (Henkel et al. 1993) and $^{16}\text{O}/^{18}\text{O} = 150$ (Harrison et al. 1999).

C.9. Hydroisocyanic acid: HNC

Similar to HCN, the $J = 2 - 1$ transition of HNC at 181.3 GHz lies outside the frequency range of the survey. We identify a feature at 174.1 GHz as the $J = 2 - 1$ transition of HN^{13}C . The detection is uncertain and thus tentative as the line is strongly blended with the also tentatively identified $3_{1,2} - 2_{1,1}$ transition of $\text{c-C}_3\text{H}$ (Sect. C.18).

C.10. Ethynyl: C_2H

The $J = 2 - 1$ group of hyperfine transitions of C_2H , observed at 174.7 GHz near the upper frequency cutoff of the survey, is the second brightest feature observed in the 2 mm window after CS. Even though the hyperfine structure is unresolved, it is still possible to differentiate the two velocity components at 160 and 280 km s^{-1} .

C.11. Thioxoethenylidene: C_2S

The survey shows four faint lines of thioxoethenylidene (131.6, 140.2, 142.5 and 144.2 GHz). The low intensity of the observed transitions makes the fitting uncertain (see Table 1). Only the $11_{10} - 10_9$ and $10_{11} - 9_{10}$ transitions at 131.6 GHz and 140.2 GHz are reliably detected, while the transitions at 142.5 GHz and 144.2 GHz are tentative.

C.12. Carbon oxide sulfide: OCS

Two transitions of carbon oxide sulfide (133.8 and 145.9 GHz) are detected in the survey. In the rotation diagram in Fig. 5 these observations are complemented by the 3 mm OCS transitions presented by Martín et al. (2005).

The $J = 13 - 12$ transition of OCS at 158.1 GHz might have been detected close to a SO_2 line, but the signal-to-noise ratio is not high enough for a reliable Gaussian fit.

C.13. Sulfur dioxide: SO_2

Five transitions of sulfur dioxide (134.0, 135.7, 140.3, 146.6 and 151.4 GHz) have been identified. The upper energy levels of the transitions range from 12 to 43 K providing a good estimate of the rotation temperature.

The $5_{1,5} - 4_{0,4}$ transition at 135.7 GHz is blended with a ^{34}SO line (Sect. C.4). Velocity and width of the line were fixed to perform a two Gaussian fit for the SO_2 and ^{34}SO transitions.

The $2_{2,0} - 2_{1,1}$ line at 151.4 GHz is contaminated by emission of a much fainter $\text{c-C}_3\text{H}_2$ line which, according to its estimated intensity (Sect. C.21), would account for $\sim 15\%$ of the observed feature. The contribution of the $\text{c-C}_3\text{H}_2$ strongly depends on the assumed T_{rot} . If we consider the uncertainty in the T_{rot} derived from $\text{c-C}_3\text{H}_2$ and estimate the contribution of this transition to the observed SO_2 line, the effect on the derived SO_2 parameters would be of ± 1 K in T_{rot} and $\pm 5\%$ in the column density.

The $5_{2,4} - 5_{1,5}$ and $7_{1,7} - 6_{0,6}$ transitions are blended with a CH_3OH group of lines at 165.1 GHz. We have estimated their contribution to the observed feature by assuming a $T_{\text{rot}} = 15$ K as derived from the rotation diagram.

For the derived excitation conditions of SO_2 , its $3_{2,2} - 3_{1,3}$ line at 158.1 GHz is expected to have an intensity of ~ 5 mK, which is below the noise level at this frequency.

C.14. Formaldehyde: H_2CO

Two ortho (140.8 and 150.5 GHz) and one para (145.6 GHz) $J = 2 - 1$ transitions of formaldehyde are detected. In each of the profiles, the two velocity components at 180 and 285 km s^{-1} are clearly separated.

The $2_{0,2} - 1_{0,1}$ transition at 145.6 GHz and the $2_{1,1} - 1_{1,0}$ at 150.4 GHz are blended with an HC_3N and a $\text{c-C}_3\text{H}_2$ line, respectively. Before performing the Gaussian fits to the H_2CO features, the estimated contributions from HC_3N (Sect. C.19) and $\text{c-C}_3\text{H}_2$ (Sect. C.21) were subtracted from the spectra.

Rotation diagrams are plotted for each velocity component (Fig. 5) where rotation temperatures of 27 K and 34 K are derived for the 180 and 285 km s^{-1} components, respectively. The 285 km s^{-1} component of the $2_{1,2} - 1_{1,1}$ transition appears to have a significantly higher intensity than expected from the rotation diagram. The large intensity of the $2_{1,2} - 1_{1,1}$ line of H_2CO could be due to the contamination by an unidentified line. If this measurement is not taken into account, the resulting temperature derived for the 285 km s^{-1} component would be $28 \pm 2 \text{ K}$ while the estimated column density would be lower by $\sim 30\%$, closer to the parameters derived from the 180 km s^{-1} component.

C.15. Thioformaldehyde: H_2CS

Three transitions, all belonging to ortho-thioformaldehyde (135.3, 139.5 and 169.1 GHz), are tentatively detected.

The $4_{1,4} - 3_{1,3}$ transition is blended with the $\text{H}36\alpha$ recombination line. A Gaussian profile similar to that of the observed $\text{H}34\alpha$ line at 160 GHz (Sect. C.26) has been subtracted. We assume that the residual emission is due to H_2CS . We also find the $4_{1,3} - 3_{1,2}$ line blended with the CS $J = 3 - 2$ emission from the image band. With the known image sideband rejection at this frequency (Fig. 3), we can estimate the contribution of the CS line measured at 146.9 GHz (Sect. C.1). The resulting feature after the subtraction of the CS line is fitted by a Gaussian profile. There is a part of this feature which is not properly fitted by emission from CS and H_2CS . This may be caused by a slight difference in the observing position between this spectrum and that containing CS in the signal band, which would cause an appreciable change in the shape of the subtracted line. Contamination by a third species is unlikely. The $5_{1,5} - 4_{1,4}$ line at 169.1 GHz is not blended, but the relatively high noise level at this frequency and the presence of nearby lines makes the fit uncertain.

A rotation temperature of 11 K is determined from the rotation diagram (Fig. 5) and

is consistent with those derived from other molecules. With this rotation temperature, the $4_{0,4} - 3_{0,3}$ transition of para- H_2CS at 137.3 GHz is expected to have an intensity of ~ 6 mK. The non-detection of this line could be explained by an excitation temperature of > 20 K.

C.16. Isocyanic acid: HNCO

The two brightest lines of isocyanic acid in the covered frequency band are clearly detected (131.9 and 153.9 GHz). The 280 km s^{-1} component of the $7_{0,7} - 6_{0,6}$ transitions at 153.9 GHz is blended with a group of CH_3CCH lines. Thus the contribution of this component has been calculated by assuming the 180 and 280 km s^{-1} velocity components have the same excitation temperature. This assumption is supported by the good fit of the CH_3CCH line to the residual feature (Sect. C.25). The line observed at 154.4 GHz is tentatively identified as the 280 km s^{-1} velocity component of the $\text{HNCO } 7_{1,6} - 6_{1,5}$ transition. The $7_{1,7} - 6_{1,6}$ transition at 153.3 GHz, which should have a similar intensity, is not detected. Due to the uncertainty of this identification, this line has not been used in the analysis of the HNCO excitation conditions. Including this transition in the rotation diagram (Fig. 5) would result in a derived $T_{\text{rot}} \sim 29$ K, slightly higher than that derived for the 180 km s^{-1} velocity component, and a column density $\sim 16\%$ lower than that in Table 2.

C.17. Protonated carbon dioxide: HOCO^+

We tentatively identified two transition (149.6 and 171.0 GHz) of protonated carbon dioxide, a quasilinear molecular ion and nearly symmetric top. These are the brightest observable transitions in the 2 mm range. Only the high velocity component of both lines are detected. The large intensity observed in the $8_{1,8} - 7_{1,7}$ transitions, expected to be similar or lower than the $7_{0,7} - 6_{0,6}$, is mainly due to the uncertainties of the baseline subtraction. A rotational temperature of 12 K have been assumed to estimate an average column density with both detected transitions.

Further observations of other HOCO^+ transitions are needed to confirm the detection and constrain the excitation temperature of this molecule.

C.18. Cyclopropenylidyne: $\text{c-C}_3\text{H}$

The $3_{1,2} - 2_{1,1}$ group of transitions at 174 GHz is the only feature of $\text{c-C}_3\text{H}$ identified in the survey. Contamination by the feature by the $J = 2 - 1$ transition of HN^{13}C makes the

fitting uncertain. Thus, the velocity component were fixed to $V_{\text{LSR}} = 180$ and 280 km s^{-1} as derived for most species and the width of the lower velocity component to $\Delta v_{1/2} = 41 \text{ km s}^{-1}$ similar to that from the fitting to the high velocity one. The $4_{1,4} - 3_{1,3}$ transitions at 172.6 GHz appear to be blended with a H^{13}CN line. At 132.9 GHz , the $3_{1,3} - 2_{1,2}$ group of transitions, which is expected to be similar in intensity to those at 174 GHz , is likely present blended to a transition of CH_2NH and an also likely transition of CH_3OH , but the noise level at these frequencies do not allow us to separate these lines. Given the considered source size of $20''$ the 133 GHz line would be 20% fainter than that at 174 GHz , so beam dilution cannot account for the non-detection of these lines. Therefore, its detection, similar to the HN^{13}C line to which it is blended (Sect. C.9) is highly tentative.

C.19. Cyanoacetylene: HC_3N

Four out of the five transitions of cyanoacetylene detected in the observed frequency range ($136.5, 145.6, 154.7, 163.8$ and 172.8 GHz) appear not to be blended with any other molecular line. Two velocity components have been fitted to each line. The $J = 16 - 15$ transition at 145.6 GHz is blended with an H_2CO line. Since we have observed more HC_3N than H_2CO lines to accurately determine the physical parameters, we have estimated the relative contribution of each of the velocity components of HC_3N . For the HC_3N $J = 18 - 17$ line, where the velocity components are not clearly differentiated, the velocity of each component has been fixed. The $J = 19 - 18$ transition seems to lie above the $T_{\text{rot}} \sim 20 \text{ K}$ derived from the other observed transitions. This may indicate that the lower energy transitions would not be optically thin as blending with any other molecular line seems unlikely. Multiline observations by Mauersberger et al. (1990) (towards a position $9''$ north of our position) also noticed an excess of the higher transition lines of HC_3N . Their comparison with model computations show that two molecular components are required to explain the observed line intensities, one with $n(\text{H}_2) \sim 10^4 \text{ cm}^{-3}$ and $T_{\text{kin}} \sim 60 \text{ K}$, and a second with $n(\text{H}_2) \sim 5 \cdot 10^5 \text{ cm}^{-3}$ and $T_{\text{kin}} \sim 150 \text{ K}$. The line intensity of the $J = 17 - 16$ transition measured in this work is about half that measured by Mauersberger et al. (1990) which indicates the strong effect of a pointing offset in the total integrated intensity. However, as far as the physical parameters are concerned, the use of the $J = 19 - 18$ line, although causing a change in the determined rotation temperature of $\sim 50\%$, affects the total column density by less than a factor of 2.

C.20. Methanimine: CH_2NH

One transition of methanimine is clearly identified in the line scan. The observed profile of the $2_{1,1} - 1_{1,0}$ transition at 133 GHz is heavily affected by non linear baselines and the fit shown in Table 1 is uncertain. The $1_{1,0} - 1_{0,1}$ transition at 167 GHz, expected to have an intensity twice as large as that at 133 GHz, is not reliably detected due to the lack of sensitivity at this frequency. Although the detection seems to be clear, further observations of transitions in other frequency bands are needed to confirm this detection.

C.21. Cyclopropenylidene: $\text{c-C}_3\text{H}_2$

Three transitions of cyclopropenylidene (155.5 and 150.8 GHz) are clearly detected. However, only one transition, the $3_{2,2} - 2_{1,1}$ line at 155.5 GHz, appears not to be blended with any other line.

The $4_{0,4} - 3_{1,3}$ and $4_{1,4} - 3_{0,3}$ lines, both at 150.8 GHz, appear to be blended. A double Gaussian profile was fitted by assuming equal width and velocity and a line intensity ratio determined by their spectroscopical parameters, assuming optically thin emission.

The intensities of the other blended transitions (145.1 and 150.4 GHz) were estimated for a rotation temperature of 9 K as derived from the rotation diagram (Fig. 5). Given the small dynamic range in energies of the unblended transitions used in the rotation diagram, the estimated T_{rot} is affected by a large uncertainty (see Table 2) and, therefore, the estimates for the blended transitions are also quite uncertain. The $5_{1,4} - 5_{0,5}$ transition at 151.3 GHz with an estimated intensity of ~ 1 mK, well below the noise level of the spectra, has been calculated with the aim of estimating its contribution to the faint SO_2 transition at that frequency (Sect. C.13).

C.22. Cyanamide: NH_2CN

Only one line of cyanamide is clearly detected in the survey, the $8_{1,7} - 7_{1,6}$ transition at 161.0 GHz which appears to be partially blended with image sideband emission from H_2S . The emission of H_2S in the signal band has been corrected by the image sideband rejection and subtracted from the spectrum before fitting the NH_2CN line. The other observed lines are close to the noise level and therefore all fitted parameters are strongly affected by the baseline. The $8_{1,8} - 7_{1,7}$ transition at 158.8 GHz, seems to be blended with a SO (Sect. C.4) but the noise level does not permit a fit. The high rotation temperature of 63 K derived

from the rotation diagram (Fig. 5) depends mainly on the fainter and therefore less reliably fitted transitions. A much lower rotation temperature would lower the column density by a factor of about 2.

C.23. Methyl cyanide: CH_3CN

Two spectral features are identified as methyl cyanide transitions (147.2 and 165.6 GHz). Each of the $J - J'$ transitions of this symmetric top consist of a number of overlapped K -components ($K = 0 \dots J - 1$). Single Gaussian profiles were fitted to the observed lines. The contribution of the $K = 0$ and 1 ladders, for the low rotation temperatures derived from other high dipole moment molecules, account for $\sim 98\%$ of the line profile. Therefore the $K > 1$ contribution to the total line intensity has not been taken into account. We derive a $T_{\text{rot}} = 10$ K from the rotation diagram in Fig. 5 which has been obtained as explained in Sect. B.2.

C.24. Methanol: CH_3OH

A total of nine transitions or groups of transitions of methanol is detected in the line survey at 143.9, 145.1, 146.4, 157, 165 and 170 GHz. The transitions at 145.1 GHz are blended with the C_3H_2 $3_{1,2} - 2_{2,1}$ line whose contribution has been estimated (Sect. C.21) and subtracted from the observed feature. In the same way, the lines at 165.0 GHz are slightly blended with SO_2 transitions. The emission of these SO_2 lines, subtracted from the spectra (Sect. C.13), mainly affects the fit of the $4_{1,3} - 4_{0,4}$ transition. The $6_{-1} - 5_0$ transition of CH_3OH expected to be detected at 132.8 GHz, is heavily affected by baseline instabilities. The rotation diagram derived from the observed transitions has been plotted using both the single- and multi-transition lines as described in Sect. B.2. The derived rotation temperature is 12 K.

C.25. Methyl acetylene: CH_3CCH

Three methyl acetylene features are observed (136.7, 153.8 and 170.9 GHz). As in the case of CH_3CN each of these corresponds to a $\Delta J = 1$ transition consisting of a number of unresolved K -components (with $K = 0 \dots J - 1$). Single Gaussian profiles have been fitted to the observed profiles.

The best fit to the rotation diagram as described in Sect. B.2 results in a rotation

temperature of ~ 62 K. Given the high rotation temperature derived only contribution of transitions with $K = 0\dots 4$, which have upper level energies < 160 K, have been taken into account in the fit. For a temperature of 60 K, transitions with $K = 4$ contribute $\sim 5\%$ to the observed profiles, while higher K lines represent less than 1% of the integrated intensities. Neglecting the contribution of these higher energy transitions (i.e. assuming the whole component is dominated by the $K = 0$ transitions) would result in an overestimation of the column densities by up to a factor of 4.

C.26. Hydrogen recombination lines

Four $H\alpha$ recombination lines are present within the frequency range covered by our survey. Only one of them, $H34\alpha$, is not blended and can be fitted. The $H33\alpha$ line lies close to the $2 - 1$ line of C_2H at the upper end of the frequency range where the rms is similar to the expected intensity of the line. The $H35\alpha$ and $H36\alpha$ lines are blended with $CS\ 3 - 2$ and $H_2CS\ 4_{1,4} - 3_{1,3}$ lines, respectively. If the relation of the line flux $S_L \propto \nu_L^2$ applies at these frequencies (Puxley et al. 1997), the lines should have flux densities 20 and 30% below that measured for the $H34\alpha$ line. We have considered them to have a similar line profile as that of the measured $H34\alpha$ line given the uncertainty in the fitted intensity.

To convert the measured $H34\alpha$ line temperature into flux densities we use the conversion factor for the 30 m telescope $S/T_{MB} = 4.95$ Jy/K. Following Puxley et al. (1997), a source to beam coupling factor $(\theta_b^2 + \theta_s^2)/\theta_b^2$ has been applied for a source size $\theta_s = 7''$. We calculate an integrated line flux of $(1.08 \pm 0.08) 10^{-19}$ W m $^{-2}$. As seen in Fig. 9, this value closely follows the best fit to the relation between the integrated line flux versus frequency derived by Puxley et al. (1997). In this figure the flux of the $H34\alpha$ line is plotted together with the recombination lines observed in millimeter and centimeter wavelengths (Puxley et al. 1997, and references therein).

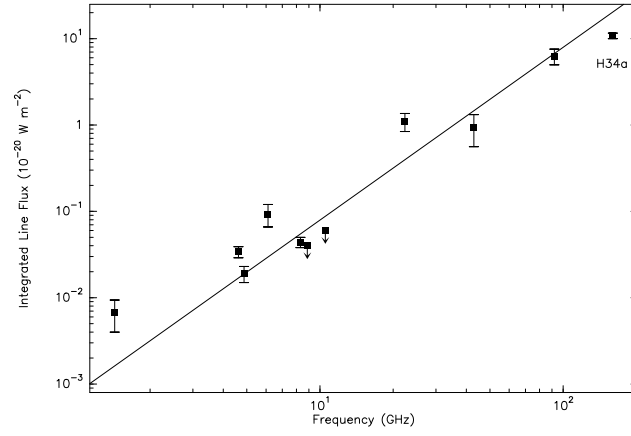


Fig. 9.— Recombination line fluxes of measured H α lines in the range from 1 to 160 GHz as a function of frequency. A best-fit to the line fluxes in the form $S_L \propto \nu^2$ is shown as fitted by Puxley et al. (1997).

REFERENCES

- Blake, G.A., Sutton, E.C., Masson, C.R., & Phillips, T.G. 1987, *ApJ*, 315, 621
- Bradford, C.M., et al. 1999, *The Universe as Seen by ISO.*, ed. P. Cox & M.F. Kessler, ESA-SP 427, 861
- Burles, S. 2002, *Plan. & Space Sci.* 50, 1245
- Canzian, B., Mundy, L.G., & Scoville, N. Z. 1988, *ApJ*, 333, 157
- Cernicharo, J., Guélin, & M., Kahane, C. 2000, *A&AS*, 142, 181
- Chin, Y.-N., Henkel, C., Millar, T.J., Whiteoak, J.B., & Mauersberger, R. 1996, *A&A*, 312, L33
- Chin, Y.-N., Henkel, C., Langer, N., & Mauersberger, R. 1999, *ApJ*, 512, L143
- Churchwell, E., Witzel, A., Huchtmeier, W., Pauliny-Toth, I.I.K., Roland, J., & Sieber, W. 1977, *A&A*, 54, 969
- Charnley, S.B., Kress, M.E., Tielens, A.G.G.M., & Millar, T.J. 1995, *ApJ*, 448, 232
- Cummins, S.E., Linke R.A., & Thaddeus P. 1986, *ApJS*, 60, 819
- Das, M., Anantharamaiah, & K.R., Yun, M.S. 2001, *ApJ*, 549, 896
- de Vaucouleurs, G., et al., 1991, *Third Reference Catalogue of Bright Galaxies*, Springer
- de Vicente, P., Martín-Pintado, J. & Wilson, T.L. 1997, *A&A*, 320, 957
- Downes, D. Radford, S.J.E., Guilloteau, S., Guélin, M., Greve, A., & Morris, D. 1992, *A&A*, 262, 424
- Engelbracht, C.W., Rieke, M.J., & Rieke, G.H. 1998, *ApJ*, 505, 639
- Flower, D.R., Pineau des Forêts, G., & Walmsley, C.M. 1995, *A&A*, 294, 815
- Forbes, D.A. & Depoy, D.L. 1992, *A&A*, 259, 97
- Fossé, D., Cesarsky, D., Gerin, M., Lequeux, J., & Tiné, S. 2000, *ISO beyond the peaks: The 2nd ISO workshop on analytical spectroscopy*, ed. A. Salama, M. F. Kessler, K. Leech, & B. Schulz, ESA-SP 456, 91
- Frayer, D.T., Seaquist, E.R., & Frail, D.A. 1998, *AJ*, 115, 559

- Friedel, D.N., Snyder, L.E., Turner, B.E., & Remijan, A. 2004, *ApJ*, 600, 234
- Fuente, A., Martín-Pintado, J., Cernicharo, J., & Bachiller, R. 1993, *A&A*, 276, 473
- Fuente, A., Rodríguez-Franco, A., & Martín-Pintado, J. 1996, *A&A*, 312, 599
- Fuente, A., Black, J.H., Martín-Pintado, J., Rodríguez-Franco, A., García-Burillo, S., Planesas, P., & Lindholm, J. 2000, *ApJ*, 545, L113
- Fuente, A., Rodríguez-Franco, A., García-Burillo, S., Martín-Pintado, J., & Black, J.H. 2003, 406, 899
- García-Burillo, S., Martín-Pintado, J., Fuente, A., & Neri, R. 2000, *A&A*, 355, 499
- García-Burillo, S., Martín-Pintado, J., Fuente, A., & Usero, A. 2002, *ApJ*, 575, L55
- Gardner, F.F. & Whiteoak, J.B. 1974, *Nat.* 247, 526
- Goicoechea, J.R., Martín-Pintado, J., & Cernicharo, J. 2005, *ApJ*, 619, 291
- Goldsmith, P.F. & Langer, W.D. 1999, *ApJ*, 517, 209
- Harrison, A., Henkel, C., & Russell, A. 1999, *MNRAS*, 303, 157
- Hasegawa, T., Sato, F., Whiteoak, J.B., & Miyawaki, R. 1994, *ApJ*, 429, L77
- Heikkilä, A., Johansson, L. E. B., & Olofsson, H. 1999, *A&A*, 344, 817
- Henkel, C. & Bally, J. 1985, *A&A*, 150, L27
- Henkel, C., Jacq, T., Mauersberger, R., Menten, K.M., & Steppe, H. 1987, *A&A*, 188, L1
- Henkel, C., Mauersberger, R., & Schilke, P. 1988, *A&A*, 201, L23
- Henkel, C., Mauersberger, R., Wiklind, T., Hüttemeister, S., Lemme, C., & Millar, T.J. 1993, *A&A*, 268, L17
- Henkel, C., Whiteoak, J.B., & Mauersberger, R. 1994, *A&A*, 284, 17
- Henkel, C., Chin, Y.-N., Mauersberger, R., & Whiteoak, J.B. 1998, *A&A*, 329, 443
- Henkel, C., Mauersberger, R., Peck, A.B., Falcke, H., & Hagiwara, Y. 2000, *A&A*, 361, L45
- Henkel, C., Tarchi, A., Menten, K.M., & Peck, A.B. 2004 *A&A*, 414, 117
- Ho, P.T.P., Martin, R.N., Henkel, C., & Turner, J.L. 1987, *ApJ*, 320, 663

- Hollenbach, D.J. & Tielens, A.G.G.M. 1997, *Annual Review of Astronomy and Astrophysics*, 35, 179
- Hüttemeister, S., Henkel, C., Mauersberger, R., Brouillet, N. Wiklind, T., & Millar, T.J. *A&A*, 1995, 295, 571
- Hüttemeister, S., Mauersberger, R., & Henkel, C. 1997, *A&A*, 326, 59
- Israel, F.P. & Baas, F, 2001, *A&A*, 371, 433
- Jacq, T., Baudry, A., Walmsley, C.M., & Caselli, P, 1999, *A&A*, 347, 957
- Jansen, D.J., Spaans, M., Hogerheijde, M.R., & van Dishoeck, E.F. 1995, *A&A*, 303, 541
- Johansson, L.E.B. 1991, in *Dynamics of galaxies and their molecular cloud distributions*, IAU-Symp. 146, eds. F.Combes, F.Casoli, Kluwer, p.272
- Kaifu, N., et al. 2004, *PASJ*, 56, 69
- Kerr, F.J. & Lynden-Bell, D. 1986, *MNRAS*, 221, 1023
- Lee, C.W., Cho, S-H., & Lee, S-M. 2001, *ApJ*, 551, 333
- Lovas, F.J. 1992, *J. Phys. Chem. Ref. Data*, 21, 181
- Lovas, F.J. 2004, *J. Phys. Chem. Ref. Data*, 33, 177
- Magain, P. & Gillet, D. 1987, *A&A*, 184, L5
- Martin,R.N. & Ho, P.T.P 1979, *A&A*, 74, L7
- Martín, S., Mauersberger, R., Martín-Pintado, J., Garca-Burillo, S., & Henkel, C. 2003, *A&A*, 411, L465
- Martín, S., Martín-Pintado, J., Mauersberger, R., Henkel, C., & Garca-Burillo, S. 2005, *ApJ*, 620, 210
- Martín-Pintado, J., Bachiller, R., & Fuente, A. 1992, *A&A*, 254, 315
- Martín-Pintado, J., de Vicente, P., Fuente, A., & Planesas, P. 1997, *ApJ*, 482, L45
- Martín-Pintado, J., Gaume, R., Rodríguez-Fernández, N.J., de Vicente, P., & Wilson, T.L. *ApJ*, 1999, 519, 667
- Martín-Pintado, J., Rizzo, J.R., de Vicente, P., Rodríguez-Fernández, N.J., & Fuente, A. 2001, *ApJ*, 548, L65

- Mattila, S. & Meikle, W.P.S. 2001, MNRAS, 324, 325
- Mauersberger & Henkel 1989, A&A, 223, 79
- Mauersberger, R., Henkel, C., & Sage, L.J. 1990, A&A, 236, 63
- Mauersberger & Henkel 1991, A&A, 245, 457
- Mauersberger, R., Henkel, C. Walmsley, C.M., Sage, L.J., & Wiklind, T. 1991, A&A, 247, 307
- Mauersberger, R., Henkel, C. 1993, Rev. Modern Astron. 6, 69
- Mauersberger, R., Henkel, C., & Chin, Y.-N. 1995, A&A, 294, 23
- Mauersberger, R., Henkel, C., Wielebinski, R., Wiklind, T., & Reuter, H.-P. 1996, A&A, 305, 421
- Mauersberger, R., Henkel, C., Weiß, A., Peck, A.B., & Hagiwara, Y. 2003, A&A, 403, 561
- McGonagle, D., Irvine, W.M., & Ohishi, M. 1994, ApJ, 422, 621
- Meier, D.S & Turner, J.L. 2005, ApJ, 618, 259
- Millar, T.J. 2002, Plan. & Space Sci. 50, 1189
- Minh, Y.C., Ziurys, L.M., Irvine, W.M., & McGonagle, D. 1991, ApJ, 366, 192
- Mouhcine, M., Ferguson, H.C., Rich, R.M., Brown, T.M., & Smith, T.E. 2005 (astro-ph/0510252)
- Nummelin, A., Bergman, P., Hjalmarson, Å., Friberg, P., Irvine, W.M., Millar, T.J., Ohishi, M., & Saito, S. 1998, ApJS, 117, 427
- Nummelin, A., Bergman, P., Hjalmarson, Å., Friberg, P., Irvine, W.M., Millar, T.J., Ohishi, M., & Saito, S. 2000, ApJS, 128, 213
- Nguyen-Q-Rieu, Nakai, N., Jackson, J.M. 1989, A&A, 220, 57
- Nguyen-Q-Rieu, Henkel, C., Jackson, J.M., & Mauersberger, R. 1991, A&A, 241, L33
- Nguyen-Q-Rieu, Jackson, J.M., Henkel, C., Truong-Bach, & Mauersberger, R. 1992, ApJ, 399, 521
- Ohishi, M., Irvine, W. M., & Kaifu, N. 1992, in IAU Symp. 150, Astrochemistry of Cosmic Phenomena, ed. P.D. Singh (Dordrecht: Kluwer), 171

- Ott, J., Weiss, A., Henkel, C., & Walter, F. 2005, *ApJ*, 629, 767
- Paglionone, T.A.D., Tosaki, T., & Jackson, J.M. 1995, *ApJ*, 454, L117
- Paglionone, T.A.D., Yam, O., Tosaki, T., & Jackson, J.M. 2004, *ApJ*, 611, 835
- Pence, W.D. 1981, *ApJ*, 247, 473
- Peng, R., Zhou, S., Whiteoak, J. B., Lo, K. Y., & Sutton, E. C. 1996, *ApJ*, 470, 821
- Petuchowski, S.J. & Bennett, C.L. 1992, *ApJ*, 391, 137
- Pety, J., Teyssier, D., Fosse, D., Gerin, M., Roueff, E., Abergel, A., Habart, E., & Cernicharo, J. 2005, *A&A*, 435, 885
- Pickett, H.M., et al. 1998, *J. Quant. Spectrosc. & Rad. Transfer* 60, 883
- Pineau des Forêts, G., Roueff, E., & Flower, D.R. 1989, *MNRAS* 240, 167
- Puche D., Carignan, C., & van Gorkom, J.H. 1991, *AJ*, 101, 456
- Puxley, P.J., Mountain, C.M., Brand, P.W.J.L., Moore, T.J.T., & Nakai, N. 1997, *ApJ*, 485, 143
- Requena-Torres, M.A., Martín-Pintado, J., Rodríguez-Franco, A., Martín, S., Rodríguez-Fernández, N. J., & de Vicente, P., 2005, submitted
- Rieke, G.H., Lebofsky, M.J., Thompson, R.I., Low, F.J., & Tokunaga, A.T. 1980, *ApJ*, 238, 24
- Rickard, L.J., Palmer, P., Morris, M., Zuckerman, B., & Turner, B.E. 1975, *ApJ*, 199, L75
- Rickard, L.J., Palmer, P., Turner, B.E., Morris, M., & Zuckerman, B. 1977, *A&A*, 214, 390
- Rodríguez-Fernández, N.J., Martín-Pintado, J., Fuente, A., & Wilson, T.L. 2004, *A&A*, 427, 217
- Rodríguez-Fernández, N.J. & Martín-Pintado, J. 2005, *A&A*, 429, 923
- Sage, L.J., Henkel, C., & Mauersberger, R. 1991, *A&A*, 249, 31
- Sage, L.J. & Ziurys, L.M. 1995, *ApJ*, 447, 625
- Sandage, A.R. & Tammann, G.A. 1987, *A Revised Shapley-Ames Catalog of Bright Galaxies*, 2nd ed. (Carnegie Institution, Washington DC)

- Sato, F., Hasegawa, T., Whiteoak, J.B., & Miyawaki, R. 2000, *ApJ*, 535, 857
- Schilke, P., Pineau des Forêts, G., Walmsley, C.M., & Martín-Pintado, J. 2001, *A&A*, 372, 291
- Scoville, N.Z., Solomon, P.M., & Penzias, A.A. 1975, *ApJ*, 201, 352
- Scoville, N.Z., Soifer, B.T., Neugebauer, G., Matthews, K., Young, J.S., & Yerka, J. 1985, *ApJ*, 289, 129
- Sequist, E.R. & Bell, M.B. 1986, *ApJ*, 303, L67
- Soifer, B.T., Boehmer, L., Neugebauer, G., & Sanders, D.B. 1989, *AJ*, 98, 766
- Sofue, Y., 1990, *PASJ*, 42, 827
- Solomon, P.M. & de Zafra, R. 1975, *ApJ*, 199, L79
- Stark, A.A. & Wolff, R.S. 1979, *ApJ*, 229, 118
- Strickland, D. K., Heckman, T. M., Colbert, E. J. M., Hoopes, C. G., & Weaver, K. A. 2004, *ApJ*, 606, 829
- Takano, S., Nakai, N., & Kawaguchi, K. 1995, *PASJ*, 47, 171
- Takano, S., Nakai, N., & Kawaguchi 2002, *PASJ*, 54, 195
- Thompson, R.I., Lebovski, M.J., & Rieke, G.H. 1978, *ApJ*, 222, L49
- Turner, B.E. 1985, *ApJ*, 299, 312
- Turner, B.E. 1989, *ApJS*, 70, 539
- Turner, B.E. 1991, *ApJS*, 76, 617
- Ulvestad, J.S & Antonucci, R.R.J. 1997, *ApJ*, 488, 621
- Usero, A., García-Burillo, S., Fuente, A., Martín-Pintado, J., & Rodríguez-Fernández, N.J. 2004, *A&A*, 419, 897
- Vidal-Madjar, A. 2002, *Plan. & Space Sci.* 50, 1161
- Wang, M., Henkel, C., Chin, Y.-N., Whiteoak, J., Cunningham, M., Mauersberger, R., & Muders, D. 2004, *A&A*, 422, 883
- Wei, A., Neininger, N., Henkel, C., Stutzki, J., & Klein, U. 2001, *ApJ*, 554, L143

- Weliachew , L. 1971, ApJ, 167, L47
- Whiteoak, J.B., Gardner, F.F., & Höglund, B. 1980, MNRAS, 190, 17
- Wild, W. 1990 Ph.D. thesis, Ludwig-Maximilian-Universität, München
- Wyrowski, F., Schilke, P., & Walmsley, C.M. 1999, A&A, 341, 882
- Zinchenko, I., Henkel, C., & Mao, R.Q. 2000, A&A, 361, 1079
- Ziurys, L.M., Friberg, P., & Irvine, W.M. 1989, ApJ, 343, 201